# Phanerozoic icehouse climates as the result of multiple solid-

1

2	Earth cooling mechanisms
3	Andrew S. Merdith <sup>1,2,*</sup> ; Thomas M. Gernon <sup>3</sup> ; Pierre Maffre <sup>4,5</sup> ; Yannick Donnadieu <sup>4</sup> ; Yves
4	Goddéris <sup>5</sup> ; Jack Longman <sup>6</sup> , R. Dietmar Müller <sup>7</sup> ; Benjamin J. W. Mills <sup>2</sup>
5	
6	1 School of Physics, Chemistry and Earth Sciences, University of Adelaide, Adelaide,
7	Australia
8	2 School of Earth and Environment, University of Leeds, Leeds LS3 9JT, UK.
9	3 School of Ocean and Earth Sciences, University of Southampton, Southampton, UK
10	4 Aix-Marseille Univ, CNRS, IRD, INRA, Coll. France, CEREGE, Aix-en-Provence, France
11	5 Géosciences-Environnement Toulouse, CNRS-Université Paul Sabatier, Toulouse, France
12	6 School of Geography and Environmental Sciences, Northumbria University, Newcastle-
13	upon-Tyne, UK
14	7 EarthByte Group, School of Geosciences, University of Sydney, NSW, Australia
15	
16	Corresponding author: andrew.merdith@adelaide.edu.au
17	
18	Abstract
19	
20	The Phanerozoic climate has been interrupted by two long 'icehouse' intervals,
21	including the current icehouse of the last ~34 million years. While these cool intervals
22	correspond to lower atmospheric CO2, it is unclear why CO2 levels fell, with hypotheses
23	suggesting changes in CO2 degassing rates or modification of silicate weathering through
24	changing continental lithology or paleogeography. Here, we construct an Earth System Model
25	that integrates these proposed cooling mechanisms in detail. The model can reproduce the

broad geologic record of ice cap expansion, allowing us to infer the primary drivers of long-term climate change. Our results indicate that recent icehouse climates required a combination of different cooling mechanisms acting simultaneously and were not driven by a single known process, potentially explaining why icehouses have been rarer than greenhouses over Earth history.

#### One sentence summary

Earth's climate swings between greenhouse and icehouse states, with icehouses occurring when multiple cooling mechanisms combine.

## INTRODUCTION

#### **Long-term drivers of climate**

Atmospheric CO<sub>2</sub> levels control global temperature variations over geologic time, with the concentration of CO<sub>2</sub> over these timescales determined by the long-term carbon cycle (I–3). Several fundamental tectonic drivers of the carbon cycle over 10–100 million-year (Ma) timescales have been proposed over the last forty years, which tend to be partly dependent on one another. Degassing of the Earth's lithosphere adds CO<sub>2</sub> to the atmosphere (4–6). Weathering of silicate minerals—especially those exposed in continental arcs (5, 7, 8) or ophiolite-bearing suture zones (9)—removes CO<sub>2</sub> from the atmosphere and ultimately buries it as carbonate minerals (10). Weathering also liberates nutrients needed for photosynthesis, which draws down atmospheric CO<sub>2</sub> and sequesters carbon as organic matter (11–13).

Changes to the Earth system through the Phanerozoic have fundamentally modified how these burial, degassing, and weathering processes operate. The most notable example is the evolution and colonization of Earth's surface by land plants during the Silurian–Devonian, which irrevocably changed both the carbon cycle and weathering processes (14–16). Since this

enhancement of weathering intensity and organic carbon burial by the emergence of land plants, subsequent variations in the carbon cycle are thought to have been driven primarily by the paleogeographic and paleotectonic evolution of Earth's continents. The slow movement and shifting of the continents have caused variations in the CO<sub>2</sub> degassing flux (17), changed patterns of global precipitation and runoff (18), and exposed different lithologies to enhanced weathering in the tropics (7–9, 19, 20). The intersection of these different mechanisms is hypothesized to control the overall degassing and weathering fluxes that set surface temperatures on Earth. Many studies have sought to reconstruct these processes over the Phanerozoic and a succession of 'Earth System' or biogeochemical models have attempted to integrate some combination of these mechanisms to reproduce the Phanerozoic CO<sub>2</sub> or temperature record and identify the drivers of key climatic excursions (2, 21–24) (fig. S1).

Empirical studies of the long-term carbon cycle have linked the temporal occurrence of continental arc degassing to climate warmth (5), their weathering to cooling (8) and the occurrence of low-latitude ophiolite bearing sutures have also been linked to cooling events (9). Modeling studies have suggested that mountain uplift events could also have driven climatic cooling (25, 26). However, there remains little agreement on which processes are most important for causing icehouse intervals as we lack a continuous Earth System Model (ESM) that can disentangle how all these processes combine to drive observed changes. Continuous, global biogeochemical models for the Phanerozoic, such as *GEOCARB(SULF)* (2, 22) and *COPSE* (Carbon-Oxygen-Phospherous-Sulfur Evolution) (21, 27) have attempted to integrate these weathering and degassing processes but are non-dimensional and not spatially explicit and therefore cannot track the spatial distribution of weatherable lithologies or hydrology through time. Further, they are unable to spatially resolve global temperature. As a result of these limitations, previous models cannot adequately reproduce the cycles between icehouses and greenhouses evident in the geologic record (fig. S1). Here, we use plate tectonic modeling

and global lithological maps to reconstruct the spatial and temporal variation of solid-Earth degassing rates and weatherable lithologies from subduction-related environments. We then incorporate these variables into a long-term 3D ESM (pySCION—a verison of the SCION (Spatial, Continuous Integration) model (23) written for the python programming language) to assess the relative importance of the cooling mechanisms they represent. Due to the considerable uncertainty in the biogeography and biotic weathering ability of early plants, alongside the unusually short duration and substantial extent of the Hirnantian glaciation (28), we do not currently expand this analysis into pre-Devonian times. Although a dynamic terrestrial and marine biosphere and their organic carbon burial fluxes are included in our analysis, we do not assess here how plant colonization affected the Earth.

#### **RESULTS and DISCUSSION**

## Assessing carbon sources and sinks over geologic time

Our ESM integrates a detailed reconstruction of the global CO<sub>2</sub> degassing rate with the global paleogeography and distribution of weatherable lithologies on the continents, overcoming the limitations of previous approaches. Degassing from the Earth's mantle and lithosphere is considered the main source of atmospheric CO<sub>2</sub> over million-year timescales (6). Degassing estimates have traditionally been taken from a variety of proxies (1), but recently full-plate reconstructions made using *GPlates* have allowed for quantitative 4-D approach through the mapping of dynamic processes at subduction zones over Phanerozoic time. Using this framework, a recent study coupled thermodynamic modeling to subducted carbon inventories to quantitatively assess the mobility of carbon in downgoing slabs and degassing through the Mesozoic and Cenozoic (6). Crucially, this study was able to quantify the contribution of pelagic sediments to arc-degassing over time, which increased markedly with the evolution of pelagic calcareous nannoplankton during the Cretaceous Period. Thus, our

implementation of it as part of our degassing curve allows us to remove from our model the 'burial depth factor'—an arbitrary scaling of degassing for pre-Cenozoic times used in all carbon-cycle models (29) that represents the increasing contribution to degassing budgets from pelagic calcareous nanoplankton since the Cretaceous.

Our analysis spans the Phanerozoic and includes degassing estimates from mid-ocean ridges, continental arcs, and continental rifts (Fig. 1A). We compile estimates of present-day fluxes from the literature (see Supplementary Materials, Fig. 1B, C) and scale them to relevant tectonic processes to estimate how the carbon flux in different tectonic environments have changed through time (Fig. 1B). We use estimates of seafloor production and consumption taken from full-plate reconstructions to scale contributions from mid-ocean ridges and subduction zones, and use the lengths of peri-continental subduction zones extracted from a full-plate model (30) to scale the amount of carbon that could be released at continental-arc environments.

We deliberately omit degassing estimates from Large Igneous Provinces (LIPs), including siliceous LIPs (sLIPs) from our compiled degassing curve, as their individual volcanic activity (and inferred degassing contribution) typically spans only a few Ma (31, 32). In contrast, our focus is the 10–100 Ma variability recorded in proxy records. This does not discount the contribution to warming or perturbations to the Earth system by either LIPs or sLIPs on short (<5 Ma) timescales, where they likely cause substantial change (33, 34). Example model runs using a basic LIP degassing database (35) are shown in the Supplementary Material (fig. S14), which underscore this point. They also demonstrate how longer-lived LIPs should have lower average degassing rates, so while some may degas over intervals of >10 Ma, the modeled climate on these timescales does not show appreciable long-term changes. The degassing contribution of the Siberian Traps, which is the only LIP we include in our 'default'

model runs as it supplied an order of magnitude more  $CO_2$  than any other Phanerozoic LIP (36–38), still only led to elevated surface temperatures for <5 Ma, which are shown in the temperature proxy record (Fig. 2B, C).

Fig. 1B depicts our total carbon degassing flux (shaded blue area, black outline) relative to present-day levels. It shows 1) high CO<sub>2</sub> degassing during the Cretaceous; 2) modern levels during the late Paleozoic and Early Mesozoic, and 3) below present-day levels in the Devonian. Our uncertainty range is calculated by dividing the minimum and maximum limits from the composite curve by the 10<sup>th</sup> and 90<sup>th</sup> percentiles (respectively) at present-day (see Supplementary Materials for details). In our merged curve, diffuse degassing around continental arcs and degassing from ridges and rifts are the most significant contributors to CO<sub>2</sub> over our analysis (Fig. 1; fig. S2), though at present-day their contributions broadly overlap with degassing derived from subducted pelagic sediments (Fig. 1C). Tracking these data back through time underscores the importance of quantifying continental deformation (that is, mainly arcs and rifts) through time, as these regions plausibly contribute between 40 and 60% of the total solid-Earth degassing budget at any time (Fig. 1B, C).

In the original *SCION* model (and in *GEOCARBSULF* and *COPSE*), Earth's surface lithology is globally uniform, and a fraction of the continental area is assumed to be volcanic (35, 39). For the current model we incorporate a digital database of ophiolite-bearing sutures (9), and estimates of peri-continental subduction zones (inferred to represent the possible extent of continental arcs) extracted from a plate model (30). These are two distinct, but overlapping litho-tectonic features, with continental arcs being the surface expression of subduction-driven volcanism and ophiolitic-bearing sutures being obducted oceanic crust when two pieces of continental crust collide. For each timestep, we produce a grid overlaying the paleogeography that records the fractional content of each cell that contains either arcs (primarily intermediate

rocks) or ophiolite-bearing sutures (primarily ultramafic—mafic rocks) (see Supplementary Materials; Fig. 1D–G; fig. S4). To include important but tectonically inactive lithological and topographic features, we propagate each raster-grid of active peri-continental subduction zones by one grid-timestep (~20 Ma), thus capturing the effects of 'relict-arcs' (7). Once the arc, suture, and relict-arc grids were constructed, the contributions of each to silicate weathering through time were calibrated using an arc and suture 'enhancement factor' (AEF and SEF, respectively): a multiplier applied to the fractional content of the respective grids (the AEF is also applied to the relict arc grids). Weathering enhancement factors were calculated using a least-squares optimization on the weathering equations (40) at present-day and determining the enhancement factors necessary to best match the riverine silicate flux across major world rivers (41). This analysis found an AEF of 7 and SEF of 20 best reproduced the present-day data (table S1, fig. S4).

#### Phanerozoic proxy data

To evaluate our model, we consider four different types of proxy data (Fig. 2) that can be used to infer transitions between icehouse and greenhouse conditions: (i) ice cap latitude; (ii) global average surface temperature; (iii) low-latitude sea surface temperature, and (iv)  $pCO_2$  levels. We consider ice cap extent to be the most robust indicator of icehouse-greenhouse transitions, but because no proxy data are able to provide a perfect indication of global temperature, we present our results against all four datasets. For each of these datasets, we add a line of best fit to compare our model quantitatively, although due to data coverage, some datasets are more amenable to this than others.

Our ice cap latitude estimates combine a database of glacial deposits (42) and Phanerozoic glendonites (43), reconstructed to their paleo-coordinates using a full-plate model (30). Uncertainties in this dataset include the reconstructed latitudes (44) and the potential that

glendonite formation might reflect the upwelling of cold water rather than cold surface temperatures (43). fig. S4 depicts both datasets separately rather than combined, as in Fig. 2A.

176

177

178

179

180

181

182

183

184

185

186

187

188

189

190

191

192

193

194

195

196

197

198

199

200

Global Average Surface Temperature (GAST) estimates are taken from two recent compilations. Firstly from Scotese et al. (45), with uncertainty from Van der Meer et al. (46), who use maps of climate-sensitive lithologies through time to define paleo-Köppen belts, with shorter-term variations based on oxygen isotopes. The continuous nature of this record, and its normalisation against long-term changes in seawater oxygen isotope ratios, makes it an attractive benchmark against which to compare model results. As well as uncertainty in reconstructed latitudes, this method relies on the assumption that Köppen belts and their indicators are broadly consistent over time (Fig. 2B). We also compare our results to the most recent 'PhanDA' curve (47), which uses a data assimilation approach to combine temperature estimates from  $\delta^{18}$ O and palaeoclimate models to estimate GAST. Although this record does not correct for variations in seawater  $\delta^{18}O$  (48), there is reasonable consensus between both approaches with regard to the timings and durations of icehouses and greenhouses, despite some differences in global average temperature. The most notable deviations pertain to the trajectory of late Palaeozoic cooling between the late Devonian and late Carboniferous and the magnitude of warmth during the Cretaceous and early Cenozoic, where estimates from (47) are  $\sim$ 5–10°C warmer than those of (45) (Fig. 2B). We also plot the low-latitude  $\pm 30^{\circ}$  sea surface temperature proxy from  $\delta^{18}$ O of shelly marine fossils (49, 50). The data we use here predominantly comes from a recent compilation (51), supplemented by studies focusing on more discrete time periods (52–55) (Fig. 2C). As with PhanDA, a key uncertainty with this proxy is whether predicted warm ocean temperatures in the Early Paleozoic are realistic, or whether they reflect changing oxygen isotope composition of seawater (3, 50, 56).

A range of proxies are used to constrain past  $CO_2$  levels based on either photosynthesizing organisms (e.g., stomatal density in leaves,  $\delta^{13}C$  in liverworts and

alkenones) or on seawater pH through boron isotopes in foraminifera and pedogenic carbonates. We use three recent compilations (57-59) that provide proxy data back to the Ordovician. Uncertainty ranges for these proxies are based on different methodological steps, particularly the estimation of soil CO<sub>2</sub> levels for the paleosol record (60), and the boron isotopic composition of seawater for reconstructing paleo-pH (61).

#### Modeled Phanerozoic climate and driving mechanisms

We now run the *SCION* model through the Phanerozoic. CO<sub>2</sub> degassing follows our compiled curve in Fig. 1B, and weatherable lithologies are mapped onto the model land surface (Fig. 1D–G). We evaluate our model by comparing its prediction of the geographic extent of ice sheets against the proxies from Fig. 2A, with a secondary focus on surface temperatures and CO<sub>2</sub> levels in Fig. 1 B–D, which are less certain. *SCION* assumes that an ice sheet is present if the grid cell continental temperature of the model output has a mean annual temperature below -10 °C (e.g., 62); as a sensitivity test, we also plot the predicted ice curve for -12 °C and -8 °C. Figure 3 shows our 'default' model ensemble, which includes all processes and considers the uncertainty bounds in the CO<sub>2</sub> degassing rate and uncertainty in the background weatherability of the non-arc and non-suture continental grid cells through time. We also show the calculated Wasserstein Distance—the mean distance between two distributions—between the uncertainty range of our results and that of the proxies in each panel.

We find that the model (Fig. 3) can replicate several key features of the Phanerozoic ice cap paleolatitude record (42), showing cooling from a warm early Devonian to a Carboniferous-Permian icehouse, followed by warming into a Triassic greenhouse, cooling through the Jurassic cool interval, into a Cretaceous hothouse and finally into a Cenozoic icehouse (63–65). The model produces more mixed fits to the CO<sub>2</sub> proxy record, compiled

global average temperature record (45, 47), and low-latitude oxygen isotope record, although the uncertainty in these records is much higher. Key misfits in the combined records, identified by the model-proxy distance metrics shown at the bottom of each panel, occur during (1) in the Devonian—where ice cap expansion and CO<sub>2</sub> drop are roughly matched, but temperature proxies are not (max ~10 °C distance). (2) In the Permian, where temperature proxies are wellmatched, CO<sub>2</sub> proxies are highly variable, but the model ice cap extent is located at higher latitudes than the associated proxy record (max ~50° distance). (3) In the Early Cretaceous, where the model has temperature within the wide uncertainty in different reconstructions, but has higher CO<sub>2</sub> (and max ~3000 ppm CO<sub>2</sub> distance) and has more restricted ice caps than the geologic record suggests. (4). In the Eocene, where the model is colder and has lower CO<sub>2</sub> than the proxy records suggest. The estimation of ice-sheet extent in our model is likely complicated by the underlying paleogeographic maps. For example, the mismatch in ice-expanse during the Permian is possibly because the underlying paleogeographic-topographic model is not conducive to producing low temperatures at low latitudes, where, at this time, localized and regional topography may be more important. We note that our model predicts the iceline extending to ~60° latitude, which is reasonably consistent with the bulk of the Gondwanan ice sheet (66). Our results over the Early Triassic also differ from the GEOCLIM model (67) because we add a weathering dependency on erosion and also have abundant low-mid-latitude ophiolitic sutures at this time that appear to help drive some component of Early Triassic cooling (fig. S6).

246

247

248

249

250

226

227

228

229

230

231

232

233

234

235

236

237

238

239

240

241

242

243

244

245

Overall, despite some apparent misfits, our model makes a generally reasonable prediction of long-term greenhouse-icehouse trends at the 10–100 Ma scale within the uncertainty offered by multiple different proxy datasets. It performs better (with a mean Wasserstein distance to modeled GAST (45) of ~3.3) than the original *SCION* model

(Wasserstein distance of 4.07) and previous simpler and more idealised model frameworks (e.g., *GEOCARBSULF* and *COPSE*, Wasserstein distances of 3.41 and 4.57 respectively, fig. S1). We now seek to better understand what is driving these model predictions by examining how individual processes act to warm or cool the model climate. To do this, we systematically re-run the model with individual drivers turned off to quantify the influence of each individual driver on changing the modelled GAST curve relative to the 'default' GAST curve of (45) (Fig. 3D)—we choose this proxy curve as a reference for this section because (1) it is continuous in high resolution over the Phanerozoic (2) it does not reach a maximum beyond which it can no longer vary (e.g. 90 ° for the ice line), and (3) it is robust to changing seawater oxygen isotope compositions. We assess the impact of the climate drivers by calculating the ratio between the Wasserstein Distance of the 'default' model distribution and each individual run with a driver switched off, with the temperature distribution at each time step. This allows us to test the influence of several previously suggested drivers of Phanerozoic Icehouses (5, 14, 25) (Fig. 3E).

In our model, the Devonian–Carboniferous cooling is predominantly driven by changes in paleogeography and a decrease in degassing, though arc weathering also plays a prominent role (Fig. 3E). Both changes in palaeogeography and degassing have been individually proposed to initiate glaciation (5, 14, 25). The former through a reduction in sea level (68, 69) and emergence of continental shelves and islands (70–72). The later by a reduction in degassing that has been linked to a slow-down in subduction rates as inferred by a lull in the magmatic zircon record (5) triggering cooling. However, our model suggests that it is only through a combination of these processes acting together that an extensive icehouse could be initiated (figs. S5–8). Our results suggest that once initiated, the prolonged icehouse was maintained predominantly by the paleogeographic configuration of the Earth, wherein the low-latitude

Variscan-Hercynian Orogeny (which formed in the Permian from the collisions between Gondwana and Laurussia, to form Pangea) increased physical weathering, maintaining cool temperatures (25).

279

280

281

282

283

284

285

286

287

288

289

290

291

292

293

294

295

296

276

277

278

The warm Mesozoic climate state in our model is also most sensitive to changes in degassing and paleogeography, specifically the increase in volcanic degassing driven by the initial rifting stages of Pangea breakup between 245 and 200 Ma. Here, we recognize an interplay between both mechanisms, whereby degassing of continental rifts increases the buildup of pCO<sub>2</sub>. However, this degassing occurs without forming new ocean basins, thus, in a palaeogeographic sense, preventing an increase in supply of nutrients derived from chemical weathering (fig. S6) reaching young ocean basins, resulting in warming (although our model is not yet able to capture the full extent of this as weathering products are always assumed to reach the ocean). Arc systems and ophiolitic sutures still contribute to enhanced silicate weathering (8); however, their contribution does not change substantially over the Mesozoic as their spatial footprint remains mostly constant and their exposure is often balanced by hydrological changes (i.e., less rainfall and runoff). Our modeled warmer Mesozoic climate is punctuated by ephemeral glaciation in the Jurassic, in reasonable, but not perfect, agreement with the geologic record of glacial deposits at this time (42). Our analysis suggests that this short-term decrease in global temperature (evident in all three temperature proxy curves) and increase in high-latitude glacial deposits is mostly driven by a reduction in degassing from both rifts and mid-ocean ridges (Fig. 1) and an increase in erosion and weathering following the breakup of Pangea (fig. S6, S7).

298

299

300

297

Finally, cooling during the Late Cretaceous and Cenozoic is most sensitive to our modeled decrease in solid-Earth degassing (Fig. 2), alongside changes to paleogeography and

arc weathering. In our compiled degassing curve, the decrease is principally driven by the reduction in degassing around continental arcs, as the decrease in mid-ocean ridge degassing is offset by the increase in degassing driven by subduction of pelagic sediments over this time (6). Tighter quantifications of the contributions of diffuse degassing around arcs and rifts would potentially change these sensitivities. Changes in paleogeography, such as those resulting from the closure of the low-latitude Tethyan Ocean and formation of the Himalayas, and exposure of arcs and ophiolitic sutures around Southeast Asia, also clearly played a role in increasing the efficacy of the silicate weathering cycle (fig. S8). While previous studies have proposed each of these drivers acting in isolation to explain this climate shift (5, 19, 26), our model results suggest that all three played important roles in contributing to global cooling.

## No single driver for Phanerozoic icehouses

To further explore whether any of the key proposed processes could exert a first-order control on Phanerozoic climate, we re-run the model subject to a single climate driver (Fig. 4, figs. S9–13). As a baseline reference, we ran the model with all drivers turned off. As expected, this produces a predominantly icehouse Earth like that of the late Cenozoic (black dashed lines in Fig. 3; fig. S7). We find that when we run the model systematically with *only* each discrete driver, the model produces an overall poor fit for the Phanerozoic icehouse-greenhouse record. While the weathering of volcanic arcs is important, it does not change substantially over the Phanerozoic and, therefore, is unable to independently force major climate change (Fig. 4; fig. S15). Weathering of ophiolite-bearing sutures changes substantially but constitutes only a minor component of the total weathering budget (Fig. 4; fig. S15).

Degassing and paleogeography show a greater ability to drive climatic change when considered alone. While some of these model runs yield reasonable fits for certain time periods,

we observe numerous discrepancies with the climate record when each driver is considered in isolation (Fig. 4). Notably, these discrepancies are far greater than those observed in the 'combined drivers' model (Fig. 3). In particular, the 'degassing only' run can reproduce a Cretaceous hothouse, but it is unable to reproduce a warmer Triassic (Fig. 4). No single mechanism can reproduce a warm Devonian, with all four single-driver runs producing an ice-dominated Devonian world (Fig. 4A). This strongly suggests that over the Phanerozoic the combination and intersection of multiple, different drivers was required to drive substantial variations in climate on 10–100 Ma timescales. While these results do not negate the correlations between individual events and climatic excursions, for example, tropical exposure of sutures with global cooling (9), or the correspondence of continental arc degassing to the Mesozoic greenhouse (5), it does suggest that single processes in isolation are incapable of explaining Earth's long-term climate state.

#### **Model limitations**

Despite some of the advances that our model can provide, there remain several key limitations that should be addressed in future work. The model uses a single paleogeographic reconstruction and a single series of paleoclimate model runs to inform the climate emulator, meaning the uncertainty in these variables cannot be assessed. Moreover, the model grid times (i.e., times at which paleogeographic maps are used to drive the paleoclimate models) are quite coarse, on average spanning ~25 Ma, but at times the gap is 40–50 Ma. Two consequences of this approach are, firstly, that many key paleogeographic transitions (such as smaller terranes and blocks entering/leaving tropical zones, emergence of continental shelves, and formation of islands arcs) are missed in our modeling strategy. Machine learning has been used to try to fill these gaps, but is not capable of reproducing hydrology to a high standard (73). Secondly, we are unable to easily test alternative paleogeographic configurations, such as Pangea-A versus

Pangea B (though see discussion in (74) about a resolution to this controversy), or differing locations of terranes in the Permian Meso-Tethyan ocean. A strength of the (py)SCION framework moving forward is that as additional paleoclimate models are generated, they can be incorporated within the climate emulator in the model—irrespective of the spatial resolution—to better resolve these fundamental questions.

It is well established that the *FOAM* (Fast-Ocean-Atmosphere Model) general circulation model has a low climate sensitivity (75) and, therefore, requires more CO<sub>2</sub> to increase temperature than more modern climate models. Additionally, *FOAM* has only been run for changes in CO<sub>2</sub>, ignoring other greenhouse gases. This may be why, despite our model predicting temperatures often within the expected ranges (i.e., 15–25°C), our *p*CO<sub>2</sub> estimates are sometimes far higher than the proxy data suggest. The *FOAM* model also has quite a coarse spatial resolution (7.5° • 4.5°, corresponding to 48 longitudinal cells by 40 latitudinal cells), which is not high enough to properly differentiate finer paleogeographic features such as the opening or closing of oceanic passages. It also struggles to properly capture small-scale drainage systems, such as those that might occur on the seaward side of a continental arc. Consequently, while we consider our model capable of capturing 10–100 Ma trends, it is unable to resolve trends on a finer spatial or temporal scale, even if they might be driven by the processes that we model.

A notable biogeochemical limitation of the model is the simple treatment of the organic carbon cycle. Despite implementing a spatially resolved weathering scheme for litho-tectonic features and the silicate weathering process, the model implementation of oxidative weathering of sedimentary organic carbon is only related to local runoff, whereas erosion rate and lithology are likely also important (11, 76). Marine organic carbon burial is not calculated spatially, despite the geologic record suggesting it is heterogeneous (77), and the model also does not feature a spatially resolved dynamic vegetation model for calculating land-derived organic

carbon burial. Such a model has been developed for the Mesozoic and Cenozoic and has been shown to alter *SCION* model predictions (78), but it has not yet been developed for the Paleozoic floras. Overall, we consider that a more sophisticated paleogeography, climate emulator, and organic carbon cycle would improve the model and could help further reconcile model results with proxy data during the misfit periods that we note. However, we believe that these advancements are unlikely to reverse the major cooling or warming trends in our results, as the net effect of amplified continental weathering is still likely to be global cooling. Even though organic carbon weathering is a CO<sub>2</sub> source, it is accompanied by nutrient delivery and a reduction in atmospheric O<sub>2</sub>, which both encourage additional organic carbon burial.

We conclude that the prolonged Phanerozoic icehouses during the Carboniferous-Permian and Cenozoic were initiated and maintained through the interaction of multiple 'climate drivers' rather than being the result of a single dominant process. This helps to explain why icehouse periods have been relatively rare during Earth history, why so many different drivers have been proposed, and why icehouse-greenhouse transitions have previously proven difficult to reproduce in more simplified carbon cycle models (3). Our results suggest that changes in paleogeography, which result in spatio-temporal variations in the hydrological cycle, alongside changes in degassing, are the two most important mechanisms. Continental arc weathering intensity is substantial during warm periods, in agreement with (8), but is not able to cause an icehouse transition by itself. Our findings suggest that glacial climates on Earth depend on the interplay between multiple global processes that occur simultaneously, carrying important implications for understanding Earth's long-term habitability. The long-term temperature of our planet appears to be mechanistically regulated towards an ice-free state rather than a glacial climate

#### MATERIALS AND METHODS

402

404

405

406

407

408

409

410

411

412

413

414

415

416

417

401

403 SCION and pySCION

The model runs were performed using pySCION, a pythonic version of the SCION model (23). The underlying **SCION** model (written in MATLAB) is available at https://github.com/bjwmills/SCION. As well as porting the model to python, the framework is extended to incorporate the impact of different lithologies on the weathering equations. The pySCION model functions as an amalgamation of the COPSE biogeochemical forward model (27), and the spatially resolved GEOCLIM model (24). Here, the pySCION model utilizes the data-structure of GEOCLIM to resolve key hydrological and climate fields (e.g., runoff, temperature) at each grid-timestep to calculate erosion and weathering. However, unlike the GEOCLIM model, which is non-continuous, in between grid-timesteps the COPSE biogeochemical model is used to integrate fluxes between timesteps. Thus, pvSCION can leverage spatially resolved data through time, allowing us to interrogate the effects of longlived geologic features on the carbon cycle. The model is available as part of the submission in Supplementary Material 1. Full model equations for SCION and pySCION are provided in (23). They are also available at the original *SCION* GitHub repository.

418

419

420

421

422

423

424

425

#### *Arc and suture weathering grids*

The same approach was taken to include both continental arcs and ophiolitic-bearing sutures in the model, whereby we calculate the fractional grid area of each cell that was composed of each litho-tectonic feature that represent estimates of the spatial extent of intermediate and mafic—ultramafic rocks, respectively. For continental arcs, we used the plate model of Merdith et al. (30) (the Phanerozoic portion of this model was adopted from models in (79-81)) to extract all subduction zones within a specific distance of a polygon (representing

continental crust) at the pySCION grid times. The distances used were 250 and 436 km, which represent the mean and mean plus one standard deviation distance of arc volcanoes from trenches at the present-day (82). We refer to these arcs as 'peri-continental' arcs rather than strictly continental arcs since it is possible that our analysis includes some arc-systems that may not be geologically classified as continental arcs. For sutures, we used the database of Macdonald et al. (9), who assembled a record of ophiolite-bearing sutures arising from arccontinent collisions during the Phanerozoic. At each timestep, the maps of arcs and sutures were rasterized onto a regularly-spaced rectangular grid using the Phanerozoic reconstruction model provided in Macdonald et al. (9)—a modified version of (72, 83). A particular shortcoming with this approach is translating linear features into area representative domains (as the digitization provided is in the form of polylines). The resolution of the rasterized grid for sutures was 18.75 • 18.75 km, reflecting the scale of the maps they were taken from (1:3,750,000) (84), and is slightly finer than estimates of ophiolite thickness from other compilations, where ophiolite sheet width typically ranges between 40 and 60 km (85, 86). For the arc data, we used a coarser grid cell size of 100 km, equivalent to the order-of-magnitude of width of continental arcs from global compilations and analyses (7, 87). In addition to rasterizing the data to these fine(r) grids, we also rasterize it to the resolution of the pySCION model (48 • 40) (e.g., fig. S3). Thus, at this point of our analysis we have two grids for each of arcs and sutures (four in total), one representing the resolution of the data, and the second at the resolution of the *pySCION* model.

446

447

448

449

450

426

427

428

429

430

431

432

433

434

435

436

437

438

439

440

441

442

443

444

445

To determine the fraction of each *pySCION* grid cell we use the latitude-longitude bounds of the coarser *pySCION* resolution map (fig. S3c) to cluster the finer resolution map. For each grid cell at the coarse resolution, we sum the area of corresponding arc or sutures from the finer resolution map to calculate a fraction of the total grid cell area of the coarser

grid that is either arc or suture. Due to differences between the underlying paleogeography and the reconstruction used, coupled with the absence of a rotation file of the underlaying *SCION* paleogeography, some manual manipulation was required to better align the reconstructed sutures and arcs with their position on the land-sea masks.

In cases where sutures overlie arcs or relict-arcs we do not subtract the area contribution attributed to sutures from both arcs and relict arcs, on the basis that sutures are features that are emplaced tectonically onto existing arc systems. Conversely, in situations where arcs overlie relict-arcs, we subtract the area of active arcs from relict-arcs to prevent double counting these regions. As the resolution of our digitization of ophiolite-bearing sutures is 18.75 km, we multiply their abundance by 3, to better reflect their preserved width (e.g. see compilation by Porkoláb et al. (86)). The digitized width of arcs is roughly equivalent to their actual width, so we do not use a multiplier for their abundance.

#### Calibrating weathering

As the standard weathering in *SCION* assumes an average lithology and reactivity across the entire globe, we introduce a weathering factor to represent the enhanced weathering that is expected from silicate rich rocks. We do this by optimizing the parameters in the *SCION* weathering equations (40, 88) in the modeled 0 Ma time-slice against the present-day measured weathering flux from a series of drainage basins (40), using a least-squares optimization from the python library *SciPy*. We include in our modeled weathering flux the distribution of pericontinental arcs and ophiolitic sutures and introduce an 'arc enhancement factor' (AEF) and 'suture enhancement factor' (SEF) to the weathering equations to isolate what enhancement is necessary to match present-day weathering rates, as measured from dissolved loads in world rivers. We use the same AEF value for our enhancement of 'relict arcs'. The values we let vary,

their range, and the results of the optimization are summarized in Supplementary Table 1. Bounds for K,  $K_w$  and  $\sigma$  are taken from Maffre et al. (40).

For the AEF and SEF, we enforce a lower bound of 7 and an upper bound of 20. These enhancements were selected to reflect present-day enhanced weatherability of silicate rocks relative to an average weatherability of continental crust. The lower limit of 7 was established as minimum increased reactivity (35). We established an upper limit based on the area of pericontinental arcs and ophiolitic-bearing sutures in our model at present-day, and their total contribution to the silicate weathering cycle. It has been suggested that volcanic silicate weathering accounts for 30% of total weathering at present-day (22) on the basis of <sup>87</sup>Sr/<sup>86</sup>Sr and <sup>187</sup>Os/<sup>188</sup>Os curves. In our analysis, the combined present-day area of peri-continental arcs and ophiolitic bearing sutures is 1.5% of Earth's surface area. Thus, we infer that a 20-fold weathering enhancement is a reasonable upper limit.

To assess our optimized values for arc and sutures factors (in addition to the other parameters) we plot them against measured data from present-day (40) (fig. S3e–g). We find that our optimized enhancement factors produce a better fit to present-day riverine flux (fig. S3g) than the unoptimized run with no enhanced weathering (fig. S3f). In particular, there are no outliers that overestimate weathering, indicating that our results (and weathering enhancement factors) are likely to be conservative.

To implement these grids within the *pySCION* framework, we multiply the fractional content of each land cell that is 'ARC', 'RELICT ARC' or 'SUTURE' according to the appropriate weathering multiplier (that is, arc enhancement factor, AEF, and suture enhancement factor, SEF) using the following equations:

502 
$$\omega_{arc} = \omega_{silw} \times \left(1 + K_{arcfrac} \times (AEF - 1)\right)$$
 (1)

503

504 
$$\omega_{relictarc} = \omega_{silw} \times \left(1 + K_{relictarcfrac} \times (AEF - 1)\right)$$
 (2)

505

506 
$$\omega_{suture} = \omega_{silw} \times \left(1 + K_{suturefrac} \times (SEF - 1)\right)$$
 (3)

507

These equations are then combined as:

509

$$\delta 10 \qquad \omega_{totalsilw} = \omega_{silw} + \omega_{arc} + \omega_{relictarc} + \omega_{suture} \tag{4}$$

511

512 Degassing

513 Previous models, including COPSE (27) and GEOCARB(SULF) (89) invert 514 Phanerozoic sea-level to approximate crustal production at mid-ocean ridges, and then use that measure as a proxy for degassing (89, 90) (i.e., CO2 output from the lithosphere into the 515 516 atmosphere). To quantify degassing in our model, we divide it into five different tectonically 517 driven sources (Fig. 1a): (i) continental rifts; (ii-iv) convergent margins, including carbon 518 sourced from the (ii) subduction of carbonaceous ocean sediments, (iii) degassed from the magma chambers (either actively or passively) or (iv) degassed diffusively on the flanks of 519 520 volcanic arcs, and (v) mid-ocean ridges. Our analysis assumes that the partitioning of carbon 521 from solid earth processes within these environments is linear through time—the same 522 proportions of carbon are being emitted now as in the past, and the only factor changing this 523 amount is variation in tectonic fluxes. Our approach is therefore to treat each source of 524 degassing separately, determining firstly an appropriate present-day flux, secondly, deriving a scaling factor able to scale the present-day flux back in time, and, thirdly, combining the scaled measurements into a single 'total' degassing curve. We use the 10<sup>th</sup> and 90<sup>th</sup> percentiles of the present-day flux to divide the minimum and maximum estimates to express the degassing curve as a flux relative to present-day. When we fully preserved the present-day uncertainty (i.e., the present-day ratio of the compiled curve is the same as the present-day relative curve), our uncertainty envelope encompassed all temperatures between 15 and 25°C over the Phanerozoic.

Our final flux is assembled from the raw data before being smoothed using a Savitzky-Golay Filter with a 21 Ma moving window and polynomial order 1. Supplementary Material 2 provides the data we used and a series of *Jupyter Notebooks* to visualize the data. We selected a 21 Ma moving window as this provided a good balance to smoothing short term perturbations that could be artefacts in the underlying plate-tectonic model, while still preserving variations on a 10 Ma scale.

#### Scaling mid-ocean ridge processes

To scale the processes occurring at mid-ocean ridges, we first derive a tectonic forcing curve constrained by three (I–III) separate curves estimating a gross tectonic flux at ridges and/or subduction zones. We use the range covered by all three curves to accommodate uncertainty in gross estimates of pre-Pangea subduction and spreading flux. (I) A recent study (17) calculated a tectonic degassing curve back to 550 Ma. They used a hybrid approach of crustal consumption curves calculated from full-plate reconstructions (91) for the Mesozoic—Cenozoic, and zircon data for the Paleozoic (80, 92) (where the zircon flux is proposed as a proxy for subduction flux). For our mid-ocean ridge, we use their hybrid curve (derived from zircons and full-plate models). Our second and third estimates of tectonic flux use crustal

consumption (II) and production (III) curves from a plate model (30). We assume that over 1–10 Ma timescales crustal production (i.e., area of new seafloor created at mid-ocean ridges) is equivalent to crustal consumption (i.e., area of seafloor consumed at subduction zones), which can be demonstrated quite clearly for the last 150 Ma (6), but before this time there are differences between the two curves. We extract both crustal production and consumption curves from 550–0 Ma. To create our final tectonic forcing curve that encompasses all three individual curves, we take the group minimum and maximum across all three curves at each timestep.

#### Scaling continental arc processes

To scale the processes occurring at continental arcs, we adopt a similar approach to our method for mid-ocean ridges. We constrain continental arc flux by three separate curves (I–III), one derived from zircon spectra (17), and the second and third from the subduction flux extracted only from peri-continental subduction zones using two different distance thresholds. We deliberately refer to these arcs as 'peri-continental' rather than continental-arcs, as limitations within plate models (e.g., rigid polygons, uncertainty about extent of continental crust back in time) make it an imperfect estimate of 'true' continental-arc length. As with the mid-ocean ridge flux, we use the range covered by all three curves to accommodate uncertainty in gross estimates of continental arc flux. (I) The study of Marcilly et al. (17) also produced a degassing estimate derived completely from zircon. As their curve is explicitly defined from arc-derived zircon, we take this as a direct proxy for continental arc flux through time. Our second and third estimates of tectonic flux use crustal consumption curves from the plate model (30). However, this time we filter the subduction zones in the model by their distance to the nearest polygon in the plate model, to extract those that could plausibly be a continental arc (rather than an oceanic arc), in the same manner we applied to produce the continental arc

silicate weathering grids. We used two distance thresholds (82), representing the (II) mean distance (250 km) and (III) mean distance plus one standard deviation (436 km) from a modeled subduction zone to volcanic arc at present day. We then multiplied these lengths by the timesensitive, average convergence rate extracted from the plate model (30) to determine an estimate of minimum and maximum peri-continental arc flux. To create our best estimate of continental arc flux curve that encompasses all three individual curves, we take the group minimum and maximum across three at for each timestep.

582

583

584

585

586

587

588

589

590

591

592

593

594

595

596

597

598

599

575

576

577

578

579

580

581

## (i) Rifts

CO<sub>2</sub> can be degassed diffusely from active continental rifts by mobilization of subcrustal reservoirs and migration via extensive fault and fracture networks (93, 94). There is a large range in degassing measurements across rift environments (95), with fluxes from the Madagi-Natron Basin in East African Rift (EAR) system thought to possibly contribute up to ~1 Mt C/a (93), while the back-arc Taupo Volcanic Zone in New Zealand (which occupies a similar area to the Madagi-Natron Basin) contributes an order of magnitude less, ~0.1 Mt C/a (96). Propagating fluxes along the entire EAR lead Lee et al. (93) to propose a total rift degassing of 14–26 Mt C/a, roughly equivalent to degassing from the entire mid-ocean ridge system, though this range was re-evaluated by Hunt et al. (94) to a more conservative 1–8 Mt C/a. Werner et al. (95) suggested fluxes from other rifts could potentially add another 8–11 Mt C/a, for a total global flux of 13–16 Mt C/a (using the mean EAR value of ref. (94)), though cautioned that many more measurements are needed. Finally, Brune et al. (97) compiled a database of rift lengths for the Mesozoic-Cenozoic and estimated global fluxes of CO<sub>2</sub> from rifts at present-day. They proposed two estimates of total contribution to C from present-day rifts, a mean estimate of 54 Mt of C/a, and a conservative estimate of 13.5 Mt of C/a. The primary difference of the two measurements reflect uncertainty around the large fluxes coming from parts of the EAR relative to other rifts. As the conservative estimate of Brune et al. (97) fall reasonably well in the centre of the tentatively proposed global range of Werner et al. (95), we use their range as a conservative uncertainty estimate of rift degassing.

To scale this present-day value back through time, we use a rift-length database (98), as organized and processed in Brune et al. (97) (450–0 Ma) and extended by Merdith et al. (99) (450–1000 Ma). However, one issue with the transition between the two databases, is that the Neoproterozoic and Early Paleozoic database predominantly identifies rifts that form during continental breakup and/or terrane detachment and migration. Comparatively, the database of (98) contains these rifts, but also rifts formed in convergent settings, such as back-arc basins. This is likely a function of preservation bias, and to counteract this issue, we calculated the fraction of rifts formed in convergent settings (98), which for the period 450–0 Ma is 0.44 (i.e. on average 44% of total rift length in the database (98) formed in convergent settings and is unaccounted for in the estimate of (99)). Assuming that this proportion is constant back to 600 Ma, we applied a rift length multiplier:

$$length_{adjusted} = length \times (1 - 0.56)^{-1}$$

to the rift lengths of (99).

Finally, the rift database (98) only provides start times of each rift in the form of a geologic time period or epoch, and so an implicit assumption of our quantification is that the rifts were only active for the duration bounded by their identified geologic timescale age. This creates an issue for very young rifts, initiated since the Neogene, as their duration age (i.e., time we consider them 'active' and degassing) becomes very short relative to older rifts that might have been attributed a start age of a longer epoch. Our estimate of rift lengths drops quite abruptly from the Pliocene to present-day (~25,000 km to ~8,000 km), because rifts given ages

of 'Pliocene' or 'Pleistocene' for example, do not contribute to the present-day estimate. Therefore, when we smooth our degassing curve, we do not fix the present-day estimate, and the result is that the smoothed curve increases at present-day and reduces the influence of rifts back through time.

#### Peri-continental arc derived carbon (ii–iv)

Much work was been done on disentangling and isolating different sources to solid-Earth degassing from continental arcs (4, 100, 101). Typically, the breakdown of continental arc carbon degassing is done on the basis of temperature, separating deeply sourced magmatic carbon (>450°C) from more shallow hydrothermally-derived carbon (102–104). Here we separate carbon sourced from continental arcs into two different categories: magmatic carbon sourced deeply from either the (ii) subducting sediments or (iii) continental crust, and (iv) diffuse degassing along continental arcs (such as through soils and springs).

#### (ii–iii) Magmatic degassing

Within subduction zones, slab-derived carbon is liberated due to the warming and devolatilization of the slab and/or sediments being subducted, and liberation of carbon stored in lower crustal reservoirs (105). Carbon pathways in subduction zones are poorly constrained, and the majority of estimates of bulk carbon fluxes from these sources are based on mass-balance estimates between carbon entering a subduction zone and what is degassed (4, 100). In addition to improvements in observation of volcanic degassing over the last twenty years (e.g. 104), advancements have also involved identifying isotopic signatures of different sources (106, 107). Analyzing data from a global compilation of fluxes, Aiuppa et al. (106) isolated high temperature volcanic degassing. They argue that based on the S/C and Ba/La ratios, and LILE enrichment patterns of volcanic arcs that most of the carbon emitted from these volcanoes come from the subducting slab (68–81%), in particular, from the sediments of the subducting

slab. The remaining 19–31% of magmatic global volcanic arc emissions are thought to be sourced from assimilation of carbon reservoirs in the lower crustal column (e.g. arc magmalimestone interaction; (105)), based on their heavy enrichment in LILEs.

653

654

655

656

657

658

659

660

661

662

663

664

665

666

667

668

669

670

671

672

673

650

651

652

Volk (108) first speculated that an increase in carbon degassing through the Cretaceous-present-day must have been driven by an increase in deep-ocean carbon burial (see also 109). This hypothesis has been part of all biogeochemical models since the original GEOCARB and COPSE models (21, 29), typically referred to as the 'B-factor' (for carbon burial), and scales-down degassing prior to 140 Ma to 75% of present-day. Müller et al. (6) provided thermodynamic modeling of carbon pathways to estimate the volume of carbon sourced from subducting slabs over the Mesozoic and Cenozoic, and argued that the majority of slab-derived carbon comes from subducting sediments (total influx into overriding plate at present-day of 31-70 Mt C/a). This study, which focussed on the oceanic conveyer belt component of the deep carbon cycle, did not consider overriding crustal sources of carbon, and the atmospheric outflux (i.e. a mass balance approach between inputs into the overriding plate, and outputs measured along volcanic arcs) was calibrated by Bekaert et al. (110), who estimated 14-24 Mt C/a based on C/S ratios from (103). Müller et al. (6) ascribed the entire reservoir from subducted sediments to this amount being outgassed, however, here, as we also consider assimilated CO<sub>2</sub> from overriding carbon storage, we partition this total amount into two sources, 68–81% from the sediment estimation of Müller et al. (6) and the remainder from the overriding plate. In effect, we take the exact outgassing flux of Muller et al. from 250–0 Ma and scale it down to 68–81% (i.e., (ii) 10–19 Mt C/a at present-day). This represents the component of carbon sourced from pelagic sediments and replaces the *B-factor* in our model. Secondly, using the present-day estimate of 14–24 Mt C/a, we take the remainder 19–32% as

the present-day flux of carbonate assimilation in the overriding plate ((iii) 2–7 Mt C/a). This later range is scaled back in time through our peri-continental arc flux curve compiled above.

(iv) Diffuse or passive degassing along continental arcs

The contribution of diffuse degassing along continental arcs, such as CO<sub>2</sub> released through soils, spring lakes and vents on the flanks of volcanoes, is thought to be a large, but uncertain, contribution to tectonic degassing. We use the present-day estimates of a recent compilation (104), which suggest 14±1.5 Mt C/a are released. This estimate only pertains to diffuse, low temperature degassing on continents, and does not include contributions from other submarine sources (e.g. 111). We use our peri-continental arc flux to scale these values back in time (fig. S5).

## (v) Mid-ocean ridges

Mid-ocean ridge degassing is driven by the release of CO<sub>2</sub>, and other volatiles, from the mantle beneath a spreading ridge. In these environments, the amount of CO<sub>2</sub> released during the formation of newly formed oceanic crust is typically calculated by analyzing the ratio of CO<sub>2</sub> to another element, chiefly <sup>3</sup>He or Ba (112). Most estimates using these methods place the present-day flux at mid-ocean ridges between 10–100 Mt C yr<sup>-1</sup> ((e.g. 113)), corresponding to a mantle concentration of around 100 ppm. Keller et al. (114) used a geodynamic model to calculate the spreading-rate dependent degassing of mid-ocean ridges, given a mantle concentration of C. This was used to estimate (6) carbon degassing at mid-ocean ridges over the last 250 Ma, with a resultant present-day flux of 13±4 Mt C yr<sup>-1</sup>, using a mantle carbon concentration of 100±20 ppm (e.g. 115). In our analysis, we use the present-day derived estimate of Müller et al. (6) and compile a composite tectonic-forcing curve back to 550 Ma to scale the relative MOR degassing back in time. This is a simplification of the method of Müller et al. (6) who calculated the flux dynamically based on known spreading rates at known mid-

ocean ridges (114). However, the bulk of our analysis covers the time interval pre-Pangea breakup, thus making it impossible to employ the same method unilaterally with the same degree of confidence. Instead, we scaled the present-day estimate of Müller et al. (6) using our tectonic forcing curve.

703

699

700

701

702

## Degassing of the Siberian Traps and other (s)LIPs

704 705 706

707

708

709

710

711

712

713

714

715

716

717

718

719

720

721

722

723

724

To investigate how the rapid release of large amounts of lithospheric carbon via large igneous provinces (LIPs) may impact our model, we performed a model run including estimates of LIP degassing (a table this data is included in the supplementary model files). Our model run is a non-exhaustive compilation of Phanerozoic LIPs (35), but does include key events including the Siberian Traps, Central Atlantic Magmatic Province, Ferrar-Karoo and Deccan Traps. We also include the Whitsunday Volcanic Province, a ca. ~15 Ma long lived sLIP that formed in the Cretaceous on the eastern margin of Australia (116). The results of this model run are shown in fig. S14. We found that LIPs do not perturb the model climate on >10 Ma timeframes—which are the focus of this study. This is because LIPs are either shorter lived than 10 Ma, or if they do have longer activities (e.g. Whitsunday Province) then this leads to a lower rate of CO<sub>2</sub> injection. Some LIPs do clearly perturb the model climate on <10 Ma timescales, and the Siberian Traps causes a multi-degree warming over several million years in our model. This is because carbon release rate from this LIP is thought to be up to an order of magnitude higher than other LIPs, up to  $1 \times 10^{13}$  mol C/a (38) over ~2 Ma. For this reason, we include the Siberian Traps in our default model runs as an endmember (maximal) example. Our analysis does not preclude LIPs acting as important climate drivers on shorter timescales (e.g. through pulsed degassing), but these events are not the focus of this work.

The implementation of these LIPs into *pySCION* is done in a similar manner to previous work (117), where we include LIP degassing as a forcing that is described by a Gaussian

function, with the midpoint defined halfway through the LIPs duration, and the width set to half the duration time. The calculated  $pCO_2$  contribution from this Gaussian is then added to the degassing flux. We assume this carbon has the same isotopic composition (-5%) and model the carbon mass balance as such.

#### Isolating mechanisms

To test the influence and strength of individual mechanisms, we isolate their contributions to be consistent with what is observed at present-day.

## Sutures, arcs, and degassing

For degassing, we assign a value of '1' for each timestep, thus ensuring that degassing remains constant through time at the present-day value. For sutures and arcs, we simply set their enhancement factors to 1, so they are considered to have the average weatherability of continental crust (equivalent to the default *SCION* model).

#### *Paleogeography*

Isolating the effects of paleogeography are more difficult and to properly test this would require alternative paleogeographic (and their dependent paleoclimate) models. As a simple measure to test the effect of paleogeography on hydrology and weathering, we alter the values of the slope and runoff to be equal to the mean value of the globe at each time step and CO<sub>2</sub> step. This acts to reduce any change in gross silicate weathering, but instead spreads it across the entire land mask at any time step (rather than being concentrated in certain areas). The homogenization occurs before the calculation of any contribution of arcs, sutures, or relict arcs to the silicate weathering flux.

750751

#### References

752

- 1. R. A. Berner, *The Phanerozoic Carbon Cycle: CO2 and O2* (Oxford University Press, USA, 2004; https://play.google.com/store/books/details?id=YHw8DwAAQBAJ).
- D. L. Royer, R. A. Berner, I. P. Montañez, N. J. Tabor, D. J. Beerling, CO2 as a primary driver of Phanerozoic climate. *GSA Today* 14, 4 (2004).
- 757 3. B. J. W. Mills, A. J. Krause, C. R. Scotese, D. J. Hill, G. A. Shields, T. M. Lenton,
  758 Modelling the long-term carbon cycle, atmospheric CO2, and Earth surface temperature
- from late Neoproterozoic to present day. *Gondwana Res.* **67**, 172–186 (2019).
- 760 4. P. B. Kelemen, C. E. Manning, Reevaluating carbon fluxes in subduction zones, what goes down, mostly comes up. *Proc. Natl. Acad. Sci. U. S. A.* **112**, E3997-4006 (2015).
- N. R. McKenzie, B. K. Horton, S. E. Loomis, D. F. Stockli, N. J. Planavsky, C.-T. A.
   Lee, Continental arc volcanism as the principal driver of icehouse-greenhouse
- 764 variability. *Science* **352**, 444–447 (2016).
- R. D. Müller, B. Mather, A. Dutkiewicz, T. Keller, A. S. Merdith, C. M. Gonzalez, W.
   Gorczyk, S. Zahirovic, Evolution of Earth's tectonic carbon conveyor belt. *Nature* 605, 629–639 (2022).
- 7. C.-T. A. Lee, S. Thurner, S. Paterson, W. Cao, The rise and fall of continental arcs:
   Interplays between magmatism, uplift, weathering, and climate. *Earth Planet. Sci. Lett.* 425, 105–119 (2015).
- 771 8. T. M. Gernon, T. K. Hincks, A. S. Merdith, E. J. Rohling, M. R. Palmer, G. L. Foster, C.
  772 P. Bataille, R. D. Müller, Global chemical weathering dominated by continental arcs
  773 since the mid-Palaeozoic. *Nat. Geosci.* 14, 690–696 (2021).
- F. A. Macdonald, N. L. Swanson-Hysell, Y. Park, L. Lisiecki, O. Jagoutz, Arc-continent collisions in the tropics set Earth's climate state. *Science* 364, 181–184 (2019).
- 10. J. C. G. Walker, P. B. Hays, J. F. Kasting, A negative feedback mechanism for the longterm stabilization of Earth's surface temperature. *J. Geophys. Res.* **86**, 9776 (1981).
- 778 11. R. G. Hilton, A. J. West, Mountains, erosion and the carbon cycle. *Nat. Rev. Earth Environ.* **1**, 284–299 (2020).
- 780 12. D. J. Burdige, Burial of terrestrial organic matter in marine sediments: A re-assessment. *Global Biogeochem. Cycles* **19** (2005).
- 782 13. C. France-Lanord, L. A. Derry, Organic carbon burial forcing of the carbon cycle from Himalayan erosion. *Nature* **390**, 65–67 (1997).
- 784 14. R. A. Berner, The Rise of Plants and Their Effect on Weathering and Atmospheric CO2.
   785 Science (1997).

- 786 15. T. J. Algeo, R. A. Berner, J. B. Maynard, S. E. Scheckler, Others, Late Devonian
- oceanic anoxic events and biotic crises: "rooted" in the evolution of vascular land plants.
- 788 *GSA Today* **5**, 45–66 (1995).
- 789 16. P. Maffre, Y. Godderis, A. Pohl, Y. Donnadieu, S. Carretier, G. Le Hir, The complex
- response of continental silicate rock weathering to the colonization of the continents by
- 791 vascular plants in the Devonian. *Am. J. Sci.* **322**, 461–492 (2022).
- 792 17. C. M. Marcilly, T. H. Torsvik, M. Domeier, D. L. Royer, New paleogeographic and
- degassing parameters for long-term carbon cycle models. *Gondwana Res.* **97**, 176–203
- 794 (2021).
- 795 18. Y. Goddéris, Y. Donnadieu, G. Le Hir, V. Lefebvre, E. Nardin, The role of
- palaeogeography in the Phanerozoic history of atmospheric CO2 and climate. *Earth-Sci*.
- 797 *Rev.* **128**, 122–138 (2014).
- 798 19. Y. Park, P. Maffre, Y. Goddéris, F. A. Macdonald, E. S. C. Anttila, N. L. Swanson-
- Hysell, Emergence of the Southeast Asian islands as a driver for Neogene cooling. *Proc.*
- 800 Natl. Acad. Sci. U. S. A. 117, 25319–25326 (2020).
- 801 20. V. Lefebvre, Y. Donnadieu, Y. Goddéris, F. Fluteau, L. Hubert-Théou, Was the
- Antarctic glaciation delayed by a high degassing rate during the early Cenozoic? *Earth*
- 803 Planet. Sci. Lett. **371–372**, 203–211 (2013).
- 21. N. M. Bergman, T. M. Lenton, A. J. Watson, COPSE: A new model of biogeochemical
- 805 cycling over Phanerozoic time. *Am. J. Sci.* **304**, 397–437 (2004).
- 806 22. R. A. Berner, GEOCARBSULF: A combined model for Phanerozoic atmospheric O2
- and CO2. Geochim. Cosmochim. Acta 70, 5653–5664 (2006).
- 808 23. B. J. W. Mills, Y. Donnadieu, Y. Goddéris, Spatial continuous integration of
- Phanerozoic global biogeochemistry and climate. *Gondwana Res.*, doi:
- 810 10.1016/j.gr.2021.02.011 (2021).
- 811 24. Y. Donnadieu, Y. Goddéris, R. Pierrehumbert, G. Dromart, F. Fluteau, R. Jacob, A
- GEOCLIM simulation of climatic and biogeochemical consequences of Pangea breakup.
- 813 Geochem. Geophys. Geosyst. 7 (2006).
- 814 25. Y. Goddéris, Y. Donnadieu, S. Carretier, M. Aretz, G. Dera, M. Macouin, V. Regard,
- Onset and ending of the late Palaeozoic ice age triggered by tectonically paced rock
- 816 weathering. *Nat. Geosci.* **10**, 382–386 (2017).
- 817 26. M. E. Raymo, W. F. Ruddiman, Tectonic forcing of late Cenozoic climate. *Nature* **359**,
- 818 117–122 (1992).
- 819 27. T. M. Lenton, S. J. Daines, B. J. W. Mills, COPSE reloaded: An improved model of
- biogeochemical cycling over Phanerozoic time. *Earth-Sci. Rev.* **178**, 1–28 (2018).
- 821 28. S. Finnegan, K. Bergmann, J. M. Eiler, D. S. Jones, D. A. Fike, I. Eisenman, N. C.
- Hughes, A. K. Tripati, W. W. Fischer, The Magnitude and Duration of Late Ordovician-
- 823 Early Silurian Glaciation. *Science* **331**, 903–906 (2011).

- 29. R. A. Berner, A model for atmospheric CO sub 2 over phanerozoic time. *Am. J. Sci.* **291** (1991).
- 30. A. S. Merdith, S. E. Williams, A. S. Collins, M. G. Tetley, J. A. Mulder, M. L. Blades,
- A. Young, S. E. Armistead, J. Cannon, S. Zahirovic, R. D. Müller, Extending full-plate
- tectonic models into deep time: Linking the Neoproterozoic and the Phanerozoic. Earth-
- 829 Sci. Rev. 214, 103477 (2021).
- 31. M. T. Jones, D. A. Jerram, H. H. Svensen, C. Grove, The effects of large igneous
- provinces on the global carbon and sulphur cycles. *Palaeogeogr. Palaeoclimatol.*
- 832 *Palaeoecol.* **441**, 4–21 (2016).
- 32. I. M. Fendley, J. Frieling, T. A. Mather, M. Ruhl, S. P. Hesselbo, H. C. Jenkyns, Early
- Jurassic large igneous province carbon emissions constrained by sedimentary mercury.
- 835 *Nat. Geosci.* **17**, 241–248 (2024).
- 33. S. V. Sobolev, A. V. Sobolev, D. V. Kuzmin, N. A. Krivolutskaya, A. G. Petrunin, N. T.
- Arndt, V. A. Radko, Y. R. Vasiliev, Linking mantle plumes, large igneous provinces and
- environmental catastrophes. *Nature* **477**, 312–316 (2011).
- 839 34. P. B. Wignall, Large igneous provinces and mass extinctions. *Earth Sci. Rev.* **53**, 1–33 (2001).
- 35. B. J. W. Mills, S. J. Daines, T. M. Lenton, Changing tectonic controls on the long-term
- carbon cycle from Mesozoic to present. *Geochem. Geophys. Geosyst.* **15**, 4866–4884
- 843 (2014).
- 36. H. Svensen, S. Planke, A. G. Polozov, N. Schmidbauer, F. Corfu, Y. Y. Podladchikov,
- B. Jamtveit, Siberian gas venting and the end-Permian environmental crisis. *Earth*
- 846 Planet. Sci. Lett. 277, 490–500 (2009).
- 847 37. C. Ganino, N. T. Arndt, Climate changes caused by degassing of sediments during the
- emplacement of large igneous provinces. *Geology* **37**, 323–326 (2009).
- 38. J. Dal Corso, B. J. W. Mills, D. Chu, R. J. Newton, T. A. Mather, W. Shu, Y. Wu, J.
- Tong, P. B. Wignall, Permo–Triassic boundary carbon and mercury cycling linked to
- terrestrial ecosystem collapse. *Nat. Commun.* **11**, 1–9 (2020).
- 39. D. L. Royer, Y. Donnadieu, J. Park, J. Kowalczyk, Y. Goddéris, Error analysis of CO2
- and O2 estimates from the long-term geochemical model GEOCARBSULF. Am. J. Sci.
- **314**, 1259–1283 (2014).
- 855 40. P. Maffre, J.-B. Ladant, J.-S. Moquet, S. Carretier, D. Labat, Y. Goddéris, Mountain
- ranges, climate and weathering. Do orogens strengthen or weaken the silicate
- weathering carbon sink? Earth Planet. Sci. Lett. 493, 174–185 (2018).
- 41. J. Gaillardet, B. Dupré, P. Louvat, C. J. Allègre, Global silicate weathering and CO2
- consumption rates deduced from the chemistry of large rivers. *Chem. Geol.* **159**, 3–30
- 860 (1999).
- 42. A. J. Boucot, C. Xu, C. R. Scotese, R. J. Morley, Phanerozoic paleoclimate: an atlas of
- lithologic indicators of climate. (2013).

- M. Rogov, V. Ershova, C. Gaina, O. Vereshchagin, K. Vasileva, K. Mikhailova, A.
   Krylov, Glendonites throughout the Phanerozoic. *Earth-Sci. Rev.* 241, 104430 (2023).
- 44. T. H. Torsvik, R. Van der Voo, U. Preeden, C. Mac Niocaill, B. Steinberger, P. V.
- Doubrovine, D. J. J. van Hinsbergen, M. Domeier, C. Gaina, E. Tohver, J. G. Meert, P.
- J. A. McCausland, L. R. M. Cocks, Phanerozoic polar wander, palaeogeography and
- 868 dynamics. *Earth-Sci. Rev.* **114**, 325–368 (2012).
- 45. C. R. Scotese, H. Song, B. J. W. Mills, D. G. van der Meer, Phanerozoic
- paleotemperatures: The earth's changing climate during the last 540 million years. *Earth*
- 871 *Sci. Rev.* **215**, 103503 (2021).
- 46. D. G. van der Meer, C. R. Scotese, B. J. W. Mills, A. Sluijs, A.-P. van den Berg van
- Saparoea, R. M. B. van de Weg, Long-term Phanerozoic global mean sea level: Insights
- from strontium isotope variations and estimates of continental glaciation. *Gondwana*
- 875 Res. 111, 103–121 (2022).
- 876 47. E. J. Judd, J. E. Tierney, D. J. Lunt, I. P. Montañez, B. T. Huber, S. L. Wing, P. J.
- Valdes, A 485-million-year history of Earth's surface temperature. *Science* **385**,
- 878 eadk3705 (2024).
- 48. T. Isson, S. Rauzi, Oxygen isotope ensemble reveals Earth's seawater, temperature, and carbon cycle history. *Science* **383**, 666–670 (2024).
- 49. J. Veizer, D. Ala, K. Azmy, P. Bruckschen, D. Buhl, F. Bruhn, G. A. F. Carden, A.
- Diener, S. Ebneth, Y. Godderis, T. Jasper, C. Korte, F. Pawellek, O. G. Podlaha, H.
- Strauss, 87Sr/86Sr, δ13C and δ18O evolution of Phanerozoic seawater. *Chem. Geol.*
- **161**, 59–88 (1999).
- 885 50. J. Veizer, A. Prokoph, Temperatures and oxygen isotopic composition of Phanerozoic
- 886 oceans. Earth-Sci. Rev. 146, 92–104 (2015).
- 51. E. L. Grossman, M. M. Joachimski, Ocean temperatures through the Phanerozoic
- 888 reassessed. Sci. Rep. 12, 8938 (2022).
- 889 52. B. B. Barney, E. L. Grossman, Supplemental Material: Reassessment of ocean
- paleotemperatures during the Late Ordovician, (2022);
- 891 https://doi.org/10.1130/GEOL.S.18822950.v1.
- 53. M. J. Cramwinckel, M. Huber, I. J. Kocken, C. Agnini, P. K. Bijl, S. M. Bohaty, J.
- Frieling, A. Goldner, F. J. Hilgen, E. L. Kip, F. Peterse, R. van der Ploeg, U. Röhl, S.
- Schouten, A. Sluijs, Synchronous tropical and polar temperature evolution in the
- 895 Eocene. *Nature* **559**, 382–386 (2018).
- 54. G. A. Henkes, B. H. Passey, E. L. Grossman, B. J. Shenton, T. E. Yancey, A. Pérez-
- Huerta, Temperature evolution and the oxygen isotope composition of Phanerozoic
- oceans from carbonate clumped isotope thermometry. Earth Planet. Sci. Lett. 490, 40–
- 899 50 (2018).
- 900 55. D. Evans, N. Sagoo, W. Renema, L. J. Cotton, W. Müller, J. A. Todd, P. K. Saraswati,
- P. Stassen, M. Ziegler, P. N. Pearson, P. J. Valdes, H. P. Affek, Eocene greenhouse

- climate revealed by coupled clumped isotope-Mg/Ca thermometry. *Proc. Natl. Acad.*
- 903 *Sci. U. S. A.* **115**, 1174–1179 (2018).
- 904 56. B. J. W. Mills, Hot and cold Earth through time, *Science (New York, N.Y.)*. **385** 905 (2024)pp. 1276–1278.
- 906 57. G. L. Foster, D. L. Royer, D. J. Lunt, Future climate forcing potentially without precedent in the last 420 million years. *Nat. Commun.* **8**, 14845 (2017).
- 908 58. C. R. Witkowski, J. W. H. Weijers, B. Blais, S. Schouten, J. S. Sinninghe Damsté, 909 Molecular fossils from phytoplankton reveal secular Pco2 trend over the Phanerozoic.
- 910 *Sci Adv* **4**, eaat4556 (2018).
- 911 59. Cenozoic CO2 Proxy Integration Project (CenCO2PIP) Consortium\*†, B. Hönisch, D.
- L. Royer, D. O. Breecker, P. J. Polissar, G. J. Bowen, M. J. Henehan, Y. Cui, M.
- 913 Steinthorsdottir, J. C. McElwain, M. J. Kohn, A. Pearson, S. R. Phelps, K. T. Uno, A.
- Ridgwell, E. Anagnostou, J. Austermann, M. P. S. Badger, R. S. Barclay, P. K. Bijl, T.
- B. Chalk, C. R. Scotese, E. de la Vega, R. M. DeConto, K. A. Dyez, V. Ferrini, P. J.
- 916 Franks, C. F. Giulivi, M. Gutjahr, D. T. Harper, L. L. Haynes, M. Huber, K. E. Snell, B.
- A. Keisling, W. Konrad, T. K. Lowenstein, A. Malinverno, M. Guillermic, L. M. Mejía,
- J. N. Milligan, J. J. Morton, L. Nordt, R. Whiteford, A. Roth-Nebelsick, J. K. C.
- Rugenstein, M. F. Schaller, N. D. Sheldon, S. Sosdian, E. B. Wilkes, C. R. Witkowski,
- 920 Y. G. Zhang, L. Anderson, D. J. Beerling, C. Bolton, T. E. Cerling, J. M. Cotton, J. Da,
- D. D. Ekart, G. L. Foster, D. R. Greenwood, E. G. Hyland, E. A. Jagniecki, J. P. Jasper,
- J. B. Kowalczyk, L. Kunzmann, W. M. Kürschner, C. E. Lawrence, C. H. Lear, M. A.
- Martínez-Botí, D. P. Maxbauer, P. Montagna, B. D. A. Naafs, J. W. B. Rae, M.
- Raitzsch, G. J. Retallack, S. J. Ring, O. Seki, J. Sepúlveda, A. Sinha, T. F. Tesfamichael,
- 925 A. Tripati, J. van der Burgh, J. Yu, J. C. Zachos, L. Zhang, Toward a Cenozoic history
- 926 of atmospheric CO2. *Science* **382**, eadi5177 (2023).
- 927 60. D. O. Breecker, Z. D. Sharp, L. D. McFadden, Atmospheric CO 2 concentrations during
- ancient greenhouse climates were similar to those predicted for A.D. 2100. *Proc. Natl.*
- 929 *Acad. Sci. U.S.A.* **107**, 576–580 (2010).
- 930 61. J. W. B. Rae, Y. G. Zhang, X. Liu, G. L. Foster, H. M. Stoll, R. D. M. Whiteford,
- Atmospheric CO2 over the past 66 million years from marine archives. *Annu. Rev. Earth*
- 932 *Planet. Sci.* **49**, 609–641 (2021).
- 933 62. K. Caldeira, J. F. Kasting, Susceptibility of the early Earth to irreversible glaciation
- 934 caused by carbon dioxide clouds. *Nature* **359**, 226–228 (1992).
- 935 63. M. V. Caputo, R. O. B. dos Santos, Stratigraphy and ages of four Early Silurian through
- Late Devonian, Early and Middle Mississippian glaciation events in the Parnaíba Basin
- 937 and adjacent areas, NE Brazil. *Earth-Sci. Rev.* **207**, 103002 (2020).
- 938 64. P. E. Isaacson, E. Díaz-Martínez, G. W. Grader, J. Kalvoda, O. Babek, F. X. Devuyst,
- Late Devonian–earliest Mississippian glaciation in Gondwanaland and its biogeographic
- onsequences. Palaeogeogr. Palaeoclimatol. Palaeoecol. 268, 126–142 (2008).

- 941 65. M. Streel, M. V. Caputo, J. H. G. Melo, M. Perez-Leyton, What do latest Famennian and
- 942 Mississippian miospores from South American diamictites tell us? *Palaeobiodiversity*
- 943 and Palaeoenvironments **93**, 299–316 (2013).
- 944 66. A. J. Boucot, X. Chen, C. R. Scotese, 'Chapter 8: Permian' in *Phanerozoic*
- Paleoclimate: An Atlas of Lithologic Indicators of Climate (SEPM (Society for
- 946 Sedimentary Geology), 2013).
- 947 67. Y. Goddéris, Y. Donnadieu, A sink-or a source-driven carbon cycle at the geological
- timescale? Relative importance of palaeogeography versus solid Earth degassing rate in
- the Phanerozoic climatic evolution. *Geol. Mag.* **156**, 355–365 (2019).
- 950 68. A. Young, N. Flament, S. E. Williams, A. S. Merdith, X. Cao, R. D. Müller, Long-term
- Phanerozoic sea level change from solid Earth processes. Earth Planet. Sci. Lett. 584,
- 952 117451 (2022).
- 953 69. C. M. Marcilly, T. H. Torsvik, C. P. Conrad, Global Phanerozoic sea levels from
- paleogeographic flooding maps. *Gondwana Res.*, doi: 10.1016/j.gr.2022.05.011 (2022).
- 955 70. C. R. Scotese, An Atlas of Phanerozoic Paleogeographic Maps: The Seas Come In and
- 956 the Seas Go Out. *Annu. Rev. Earth Planet. Sci.* **49**, 679–728 (2021).
- 957 71. W. Cao, S. Zahirovic, N. Flament, S. Williams, J. Golonka, R. D. Müller, Improving
- global paleogeography since the late Paleozoic using paleobiology. *Biogeosci. Discuss.*,
- 959 1–24 (2017).
- 960 72. T. H. Torsvik, L. R. M. Cocks, Earth History and Palaeogeography (Cambridge
- University Press, 2016; https://www.cambridge.org/core/books/earth-history-and-
- palaeogeography/076D4FCFCEE4CAE6F8EF3B449594DD50).
- 963 73. D. Zheng, A. Merdith, Y. Goddéris, Y. Donnadieu, K. Gurung, B. J. Mills, Using Deep
- Learning to integrate paleoclimate and global biogeochemistry over Phanerozoic time.
- 965 Geoscientific Model Development Discussions **2024**, 1–20 (2024).
- 966 74. M. Domeier, E. Font, N. Youbi, J. Davies, S. Nemkin, R. Van der Voo, M. Perrot, M.
- Benabbou, M. A. Boumehdi, T. H. Torsvik, On the Early Permian shape of Pangea from
- paleomagnetism at its core. Gondwana Res. 90, 171–198 (2021).
- 969 75. S. Wu, Z. Liu, J. Du, Y. Liu, Change of global ocean temperature and decadal variability
- 970 under 1.5 °C warming in FOAM. J. Mar. Sci. Eng. 10, 1231 (2022).
- 971 76. J. R. Zondervan, R. G. Hilton, M. Dellinger, F. J. Clubb, T. Roylands, M. Ogrič, Rock
- organic carbon oxidation CO2 release offsets silicate weathering sink. *Nature* **623**, 329–
- 973 333 (2023).
- 974 77. Z. Li, Y. G. Zhang, M. Torres, B. J. W. Mills, Neogene burial of organic carbon in the
- 975 global ocean. *Nature* **613**, 90–95 (2023).
- 976 78. K. Gurung, K. J. Field, S. A. Batterman, S. W. Poulton, B. J. W. Mills, Geographic
- 977 range of plants drives long-term climate change. *Nat. Commun.* **15**, 1805 (2024).

- 978 79. M. Domeier, A plate tectonic scenario for the Iapetus and Rheic oceans. *Gondwana Res.* 36, 275–295 (2016).
- 980 80. M. Domeier, V. Magni, M. W. Hounslow, T. H. Torsvik, Episodic zircon age spectra mimic fluctuations in subduction. *Sci. Rep.* **8**, 17471 (2018).
- 982 81. A. Young, N. Flament, K. Maloney, S. Williams, K. Matthews, S. Zahirovic, R. D.
- Müller, Global kinematics of tectonic plates and subduction zones since the late
- Paleozoic Era. Geoscience Frontiers 10, 989–1013 (2019).
- 985 82. S. Zahirovic, A. Eleish, S. Doss, J. Pall, J. Cannon, M. Pistone, M. G. Tetley, A. Young,
- P. Fox, Subduction and carbonate platform interactions. *Geosci. Data J.*, doi:
- 987 10.1002/gdj3.146 (2022).
- 988 83. M. Domeier, Early Paleozoic tectonics of Asia: Towards a full-plate model. *Geoscience Frontiers* 9, 789–862 (2018).
- 990 84. J. Hartmann, N. Moosdorf, The new global lithological map database GLiM: A representation of rock properties at the Earth surface. *Geochem. Geophys. Geosyst.* 13

992 (2012).

- 993 85. P. Mann, A. Taira, Global tectonic significance of the Solomon Islands and Ontong Java Plateau convergent zone. *Tectonophysics* **389**, 137–190 (2004).
- 86. K. Porkoláb, T. Duretz, P. Yamato, A. Auzemery, E. Willingshofer, Extrusion of subducted crust explains the emplacement of far-travelled ophiolites. *Nat. Commun.* 12, 1499 (2021).
- 998 87. J. de Bremond d'Ars, C. Jaupart, R. S. J. Sparks, Distribution of volcanoes in active margins. *J. Geophys. Res.* **100**, 20421–20432 (1995).
- 1000 88. J. A. West, Thickness of the chemical weathering zone and implications for erosional and climatic drivers of weathering and for carbon-cycle feedbacks. *Geology* **40**, 811–1002 814 (2012).
- 89. R. A. Berner, GEOCARB II: A revised model of atmospheric CO2 over Phanerozoic time. *Am. J. Sci.* **294** (1994).
- 90. S. Gaffin, Ridge volume dependence on seafloor generation rate and inversion using long term sealevel change. *Am. J. Sci.* **287**, 596–611 (1987).
- 91. K. J. Matthews, K. T. Maloney, S. Zahirovic, S. E. Williams, M. Seton, R. D. Müller, Global plate boundary evolution and kinematics since the late Paleozoic. *Glob. Planet. Change* **146**, 226–250 (2016).
- 1010 92. M. W. Hounslow, M. Domeier, A. J. Biggin, Subduction flux modulates the geomagnetic polarity reversal rate. *Tectonophysics* **742–743**, 34–49 (2018).
- 1012 93. H. Lee, J. D. Muirhead, T. P. Fischer, C. J. Ebinger, S. A. Kattenhorn, Z. D. Sharp, G.
- Kianji, Massive and prolonged deep carbon emissions associated with continental
- 1014 rifting. *Nat. Geosci.* **9**, 145–149 (2016).

- 1015 94. J. A. Hunt, A. Zafu, T. A. Mather, D. M. Pyle, P. H. Barry, Spatially variable
- 1016 CO<sub>2</sub>degassing in the main Ethiopian rift: Implications for magma storage, volatile
- transport, and rift-related emissions. *Geochem. Geophys. Geosyst.* **18**, 3714–3737
- 1018 (2017).
- 1019 95. C. Werner, T. P. Fischer, A. Aiuppa, M. Edmonds, C. Cardellini, S. Carn, G. Chiodini,
- 1020 E. Cottrell, M. Burton, H. Shinohara, P. Allard, 'Carbon Dioxide Emissions from
- Subaerial Volcanic Regions' in *Deep Carbon: Past to Present* (Cambridge University
- Press, 2019; https://www.cambridge.org/core/books/deep-carbon/carbon-dioxide-
- 1023 emissions-from-subaerial-volcanic-
- regions/F8B4EFAE0DAF5306A8D397C23BF3F0D7), pp. 188–236.
- 1025 96. T. M. Seward, D. M. Kerrick, Hydrothermal CO2 emission from the Taupo Volcanic
- Zone, New Zealand. Earth Planet. Sci. Lett. 139, 105–113 (1996).
- 97. S. Brune, S. E. Williams, R. D. Müller, Potential links between continental rifting, CO2
- degassing and climate change through time. *Nat. Geosci.* **10**, 941–946 (2017).
- 98. A. M. C. Şengör, B. A. Natal'in, Rifts of the world. Mantle plumes: their identification,
- 1030 doi: 10.1130/0-8137-2352-3.389 (2001).
- 1031 99. A. S. Merdith, S. E. Williams, S. Brune, A. S. Collins, R. D. Müller, Rift and plate
- boundary evolution across two supercontinent cycles. *Glob. Planet. Change* **173**, 1–14
- 1033 (2019).
- 1034 100. R. Dasgupta, M. M. Hirschmann, The deep carbon cycle and melting in Earth's
- interior. Earth Planet. Sci. Lett. **298**, 1–13 (2010).
- 1036 101. P. J. Gorman, D. M. Kerrick, J. A. D. Connolly, Modeling open system metamorphic
- decarbonation of subducting slabs. *Geochem. Geophys. Geosyst.* 7 (2006).
- 1038 102. A. Aiuppa, T. P. Fischer, T. Plank, P. Bani, CO2 flux emissions from the Earth's most
- actively degassing volcanoes, 2005-2015. Sci. Rep. 9, 5442 (2019).
- 1040 103. T. P. Fischer, Fluxes of volatiles (H2O, CO2, N2, Cl, F) from arc volcanoes.
- 1041 *Geochem. J.* **42**, 21–38 (2008).
- 1042 104. T. P. Fischer, S. Arellano, S. Carn, A. Aiuppa, B. Galle, P. Allard, T. Lopez, H.
- Shinohara, P. Kelly, C. Werner, C. Cardellini, G. Chiodini, The emissions of CO2 and
- other volatiles from the world's subaerial volcanoes. Sci. Rep. 9, 18716 (2019).
- 1045 105. E. Mason, M. Edmonds, A. V. Turchyn, Remobilization of crustal carbon may
- dominate volcanic arc emissions. *Science* **357**, 290–294 (2017).
- 1047 106. A. Aiuppa, T. P. Fischer, T. Plank, P. Robidoux, R. Di Napoli, Along-arc, inter-arc
- and arc-to-arc variations in volcanic gas CO2/ST ratios reveal dual source of carbon in
- arc volcanism. *Earth-Sci. Rev.* **168**, 24–47 (2017).
- 1050 107. T. Kagoshima, Y. Sano, N. Takahata, T. Maruoka, T. P. Fischer, K. Hattori, Sulphur
- 1051 geodynamic cycle. Sci. Rep. 5, 8330 (2015).

- 1052 T. Volk, Sensitivity of climate and atmospheric CO2 to deep-ocean and shallow-1053 ocean carbonate burial. Nature 337, 637-640 (1989).
- 1054 109. K. Caldeira, Enhanced Cenozoic chemical weathering and the subduction of pelagic 1055 carbonate. Nature 357, 578-581 (1992).
- 1056 110. D. V. Bekaert, S. J. Turner, M. W. Broadley, J. D. Barnes, S. A. Halldórsson, J.
- 1057 Labidi, J. Wade, K. J. Walowski, P. H. Barry, Subduction-driven volatile recycling: A
- 1058 global mass balance. Annu. Rev. Earth Planet. Sci. 49, 37–70 (2021).
- 1059 K. A. Campbell, J. D. Farmer, D. Des Marais, Ancient hydrocarbon seeps from the
- Mesozoic convergent margin of California: carbonate geochemistry, fluids and 1060
- 1061 palaeoenvironments. Geofluids 2, 63-94 (2002).
- 1062 112. B. Marty, I. N. Tolstikhin, CO2 fluxes from mid-ocean ridges, arcs and plumes. 1063 Chem. Geol. 145, 233-248 (1998).
- 1064 113. M. M. Hirschmann, Comparative deep Earth volatile cycles: The case for C recycling
- 1065 from exosphere/mantle fractionation of major (H2O, C, N) volatiles and from H2O/Ce,
- 1066 CO2/Ba, and CO2/Nb exosphere ratios. Earth Planet. Sci. Lett. 502, 262–273 (2018).
- 1067 T. Keller, R. F. Katz, M. M. Hirschmann, Volatiles beneath mid-ocean ridges: Deep
- 1068 melting, channelised transport, focusing, and metasomatism. Earth Planet. Sci. Lett.
- 1069 **464**, 55–68 (2017).
- 1070 J. M. Tucker, S. Mukhopadhyay, H. M. Gonnermann, Reconstructing mantle carbon
- 1071 and noble gas contents from degassed mid-ocean ridge basalts. Earth Planet. Sci. Lett.
- 1072 **496**, 108–119 (2018).
- 1073 S. E. Bryan, A. Ewart, C. J. Stephens, J. Parianos, P. J. Downes, The Whitsunday
- Volcanic Province, Central Queensland, Australia: lithological and stratigraphic 1074
- 1075 investigations of a silicic-dominated large igneous province. J. Volcanol. Geotherm.
- 1076 Res. 99, 55–78 (2000).
- 1077 117. J. Longman, B. J. W. Mills, Y. Donnadieu, Y. Goddéris, Assessing volcanic controls on Miocene climate change. Geophys. Res. Lett. 49 (2022).
- 1078
- 1079 F. Crameri, G. E. Shephard, P. J. Heron, The misuse of colour in science 118.
- 1080 communication. *Nat. Commun.* **11**, 5444 (2020).
- Y. Goddéris, Y. Donnadieu, V. Lefebvre, G. Le Hir, E. Nardin, Tectonic control of 1081 119.
- 1082 continental weathering, atmospheric CO2, and climate over Phanerozoic times. C. R.
- 1083 Geosci. 344, 652–662 (2012).
- 1084 120. R. C. Blakey, 'Gondwana paleogeography from assembly to breakup—A 500 m.y.
- 1085 odyssey' in Special Paper 441: Resolving the Late Paleozoic Ice Age in Time and Space
- 1086 (Geological Society of America, 2008;
- 1087 https://books.google.com/books?hl=en&lr=&id=FCPxDyHJ-
- 1088 zIC&oi=fnd&pg=PA1&dq=Gondwana+paleogeography+from+assembly+to+breakup%
- 1089 E2%80%94A+500+m.y.+odyssey&ots=g 3p1QjaFZ&sig=Ve30DDelkTlhLPUbudi8mx
- 1090 -m1ME)vol. 441, pp. 1–28.

- 1091 121. X. Chu, C.-T. A. Lee, R. Dasgupta, W. Cao, The contribution to exogenic CO2 by contact metamorphism at continental arcs: A coupled model of fluid flux and metamorphic decarbonation. *Am. J. Sci.* **319**, 631–657 (2019).
- 1094 122. S. E. Bryan, A. G. Cook, C. M. Allen, C. Siegel, D. J. Purdy, J. S. Greentree, I. T. Uysal, Early-mid Cretaceous tectonic evolution of eastern Gondwana: From silicic LIP magmatism to continental rupture. *Episodes* **35**, 142–152 (2012).
- 1097 123. S. E. Bryan, A. E. Constantine, C. J. Stephens, A. Ewart, R. W. Schön, J. Parianos, Early Cretaceous volcano-sedimentary successions along the eastern Australian continental margin: Implications for the break-up of eastern Gondwana. *Earth Planet*. 1100 *Sci. Lett.* 153, 85–102 (1997).

### Acknowledgments

The authors thank anonymous reviewers, A. Farnsworth and C. Goldblatt for constructive criticism that improved many aspects of this study.

### **Funding**

EU MSCA-IF: 893615 (NEOEARTH). ASM, BJWM

ARC DECRA: DE230101642 (ASM)

WoodNext Foundation (TG)

#### **Author contributions:**

Writing-original draft: ASM, BJWM, YG

Conceptualisation: YD, TG, ASM, BJWM, YG, PM

Investigation: TG, ASM

Writing—review and editing: YD, DM, TG, ASM, JL, BJWM, YG

Methodology: YD, TG, ASM, JL, BJWM, YG

Resources: YD, ASM, BJWM

Funding acquisition: TG, ASM, BJWM

Data curation: ASM

Validation: DM, TG, ASM, BJWM, YG, PM

Supervision: BJWM

Formal analysis: ASM, JL

Software: ASM, JL, BJWM

Project administration: ASM, BJWM

Visualisation: ASM, BJWM

**Competing interests:** All authors declare that they have no competing interests.

Data and materials availability statement: The data used and generated in our study are

available at https://zenodo.org/record/7940113, or from the original referenced publications

discussed in text. Figures 1–4 were produced using perceptually uniform colour maps (118).

**Rights** 

For the purpose of open access, the authors have applied a creative commons attribution (CC

BY) licence to any author accepted manuscript version arising.

# **Supplementary Materials**

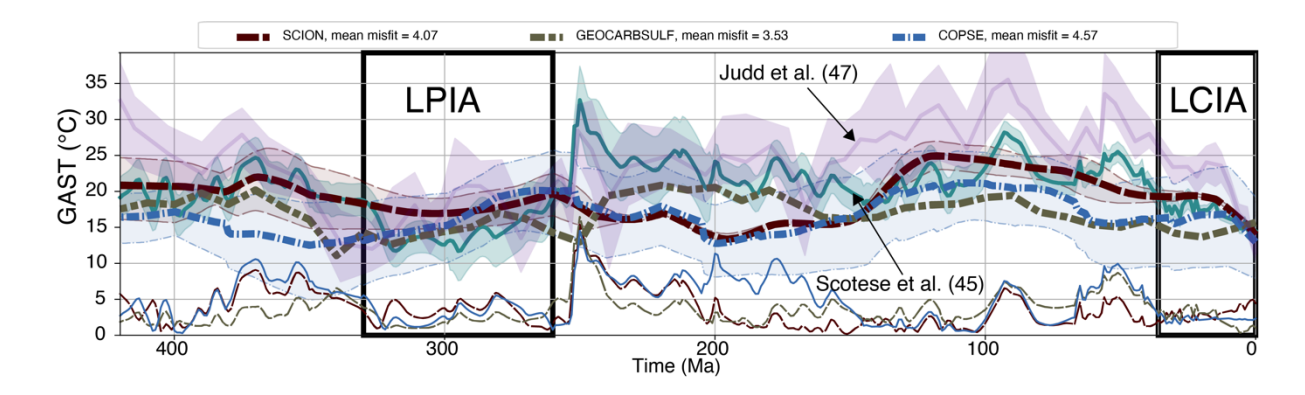
Supplementary Figures, 1–15 Supplementary Table 1

### Data s1

Summary of degassing calculations and rates from different tectonic regions used to compile our degassing curve.

### Data s2

pySCION model base-code. Requires python installation to run.



## **Figures and Figure Captions**

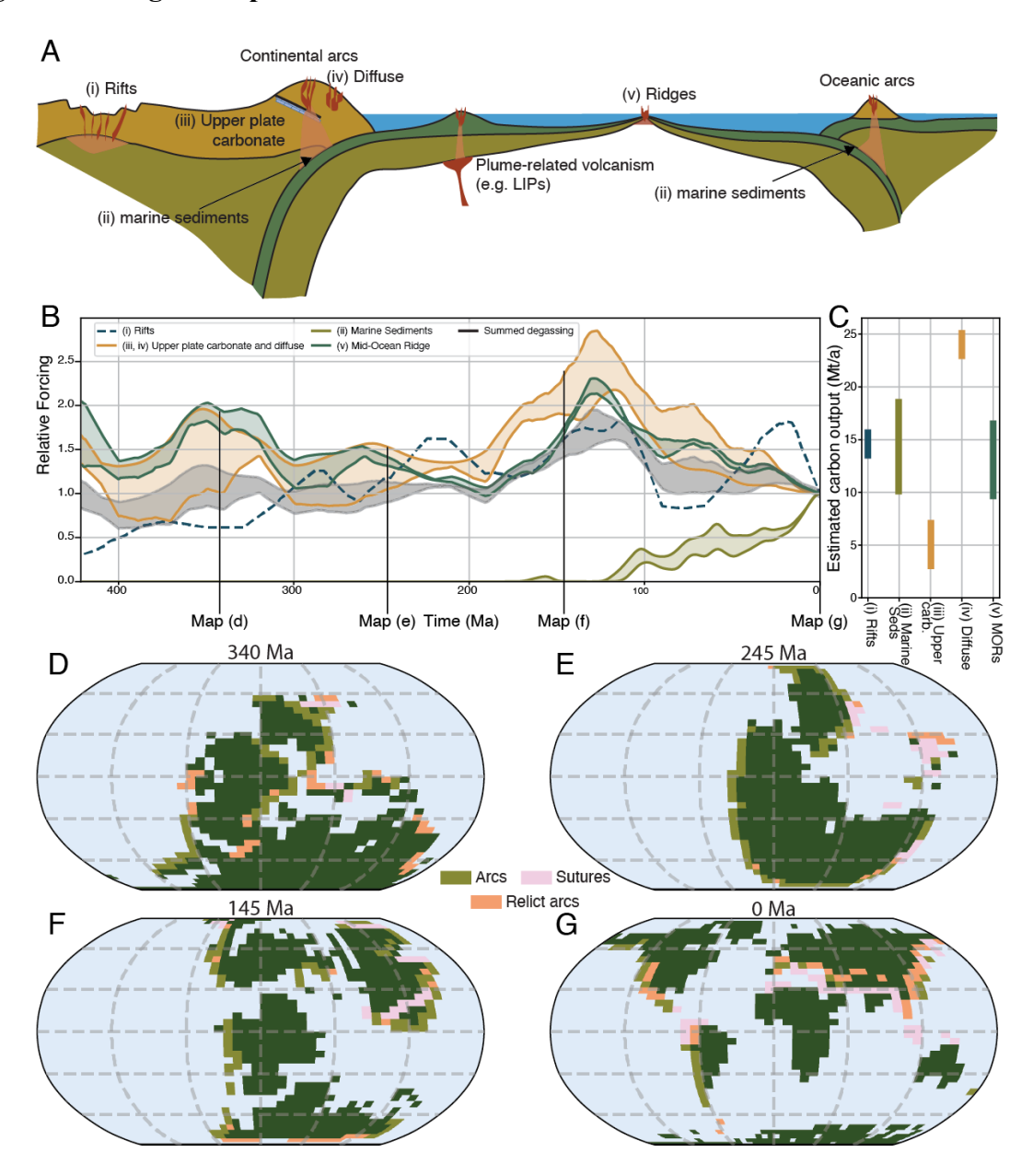


Figure 1. Sources and sinks of CO<sub>2</sub> implemented within pySCION. (A) Summary of different tectonic environments from which carbon is degassed. (B) Tectonic forcing curves that we use

to scale each individual flux back in time divided into continental rifts, continental arcs, midocean ridges, and subducting marine sediments. Our total summed curve used to drive the model is also depicted. (C) Present-day measured or modeled flux from different sources (corresponding to panel (A), including from (i) continental rifts (97, 104); (ii) from subduction of marine sediments (6, 110); (iii) assimilated from lower crustal sources on the upper plate (106); (iv) diffuse degassing from the flanks of continental arcs (104); and (v) from mid-ocean ridges (6). (D–G) spatial boundary conditions (land-sea/paleogeographic maps) (119, 120) of pySCION, depicting our lithological maps that are used to enhance the silicate weathering process.

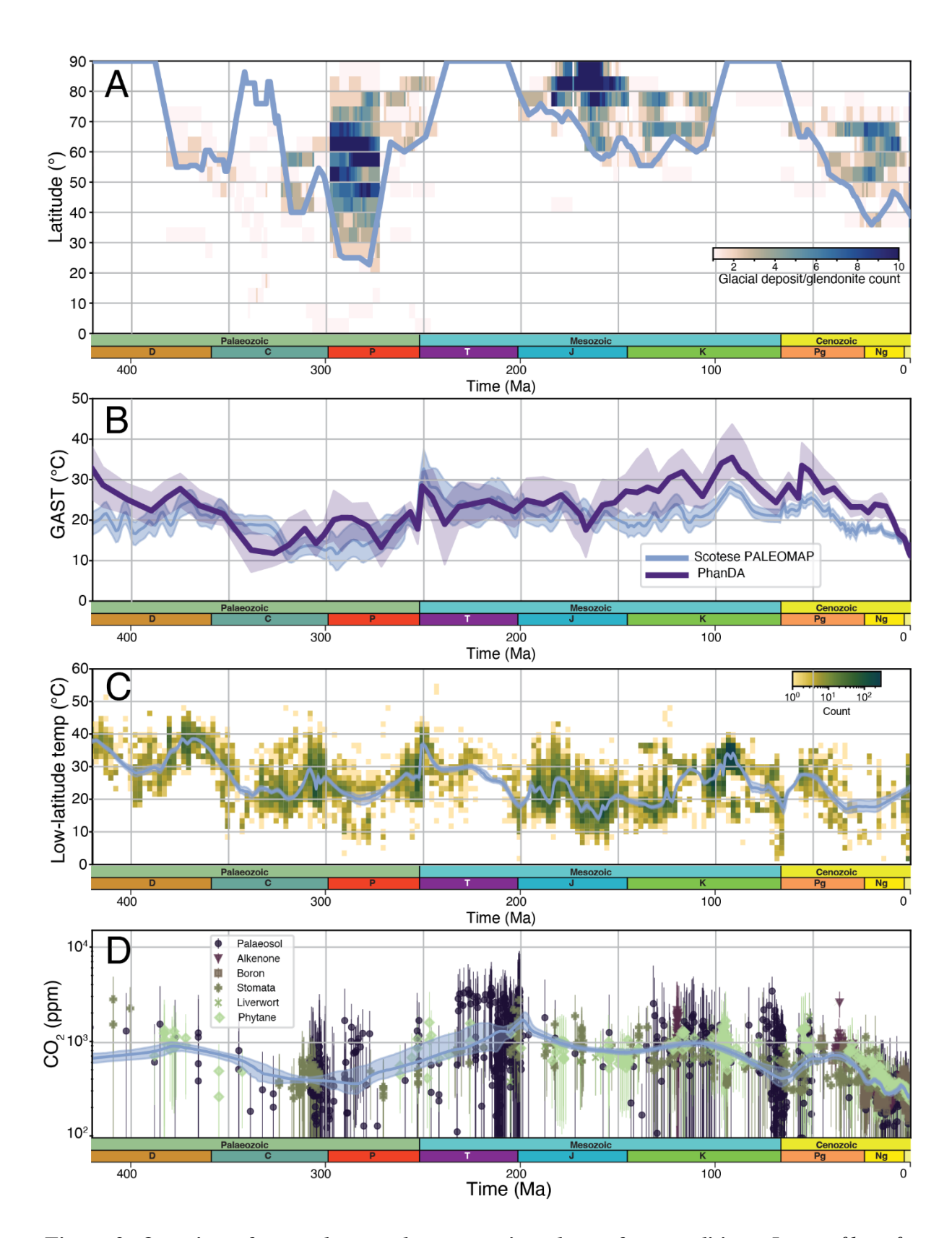


Figure 2: Overview of proxy data used to constrain paleosurface conditions. Lines of best fit are shown in each panel (in blue). (A) Iceline extent estimated from preserved lithological

indicators of cold climates (tillites, dropstones, and glendonites). The heatmap shows the temporal distribution in 10° latitudinal bins, considering the age uncertainty provided in the underlying dataset, and is colored by abundance. The maximum ice extent is a smoothed line (moving window of 11 Ma) requiring at least two or more deposits to be in a latitudinal bracket (explaining why in the Carboniferous this does not extend to 90°). For panels (C–D), a line of best fit and 95% confidence interval (solid blue line and interval) was calculated using a nonparametric locally weighted scatterplot smoothing (LOWESS) function (www.statsmodels.org). (B) GAST with uncertainty (blue line and envelope) of (45, 46) and GAST with uncertainty (2 sigma, indigo line and envelope) of (47). (C) Equatorial average surface temperature derived from oxygen isotopes (51). We have depicted the data as a heatmap to show the concentration. (D)  $pCO_2$  proxy data (57, 58).

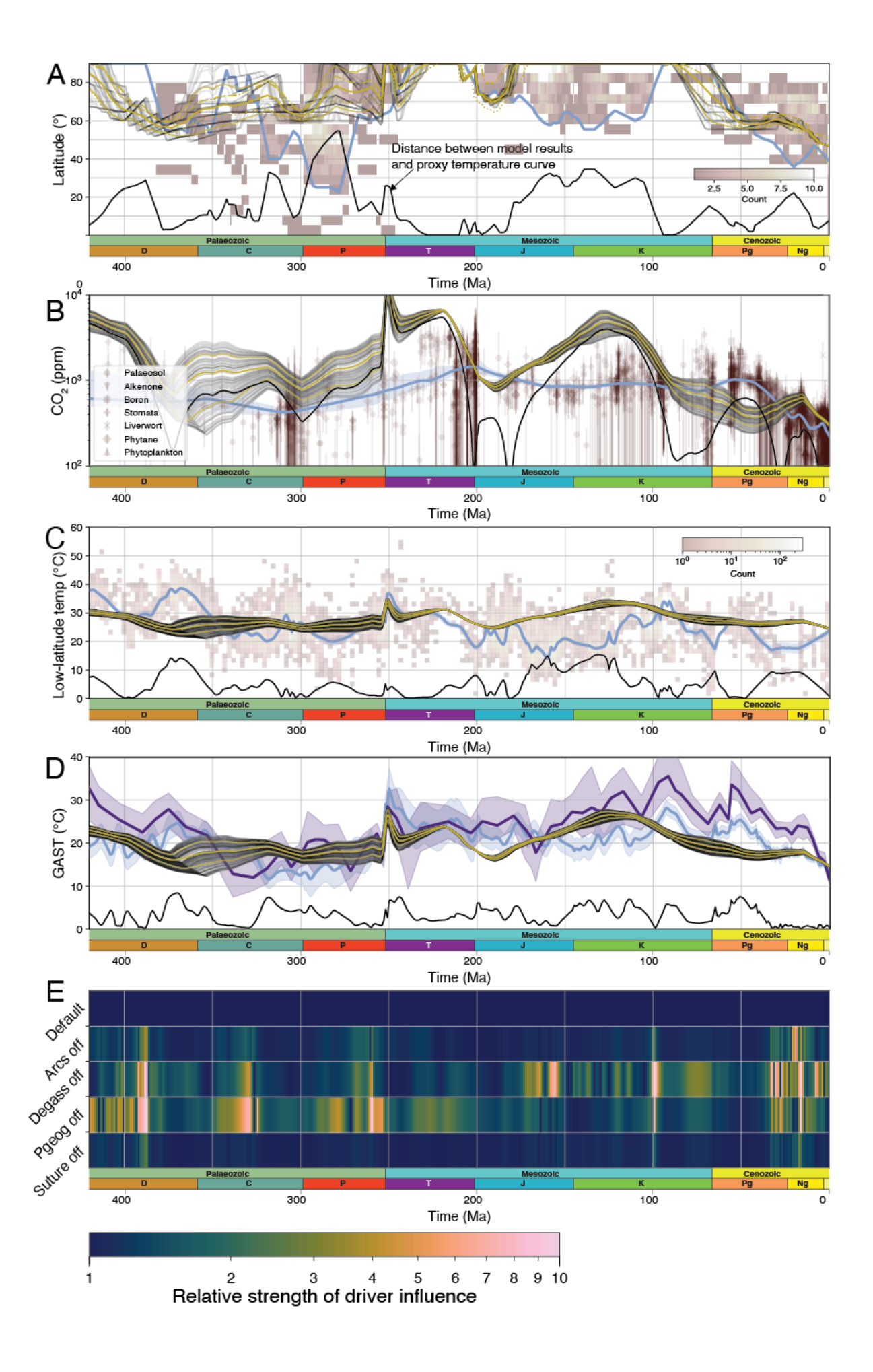


Figure 3. pySCION model results for the Phanerozoic. Results from our default run are plotted in panels (A–D), where gray lines show 10% of the ensemble (1000 runs per ensemble), and the solid amber lines are the mean  $\pm$  1 standard deviation. In some cases where ensemble runs overlap, the lines are black (e.g., panel A). For comparison, proxy data are in red-brown, and their lines of best fit and confidence are shown in blue (see Fig. 2 caption for details). Solid black lines show the distance between proxies and model. (A) Ice line results. The default model run assumes a critical temperature of -10°C, and the mean values of alternative runs assuming critical temperatures of -8°C and -12°C are represented by the coarse and fine dashed amber lines, respectively. (B)Atmospheric CO<sub>2</sub> results. (C) Modeled equatorial ( $\pm$ 30°) average surface temperature against equatorial ( $\pm$ 30°) sea-surface temperature from  $\delta$ 80 (51). (D) Global average surface temperature (GAST) and uncertainty of Scotese et al. (45) in blue, and Judd et al. (47) in indigo. (E) Relative influence of each climate driver when it is turned 'off' (no change relative to present-day)—a measure of how influential each driver is through time. Temperature, ice line, and CO<sub>2</sub> for each series of runs are provided in figs. S9–14.

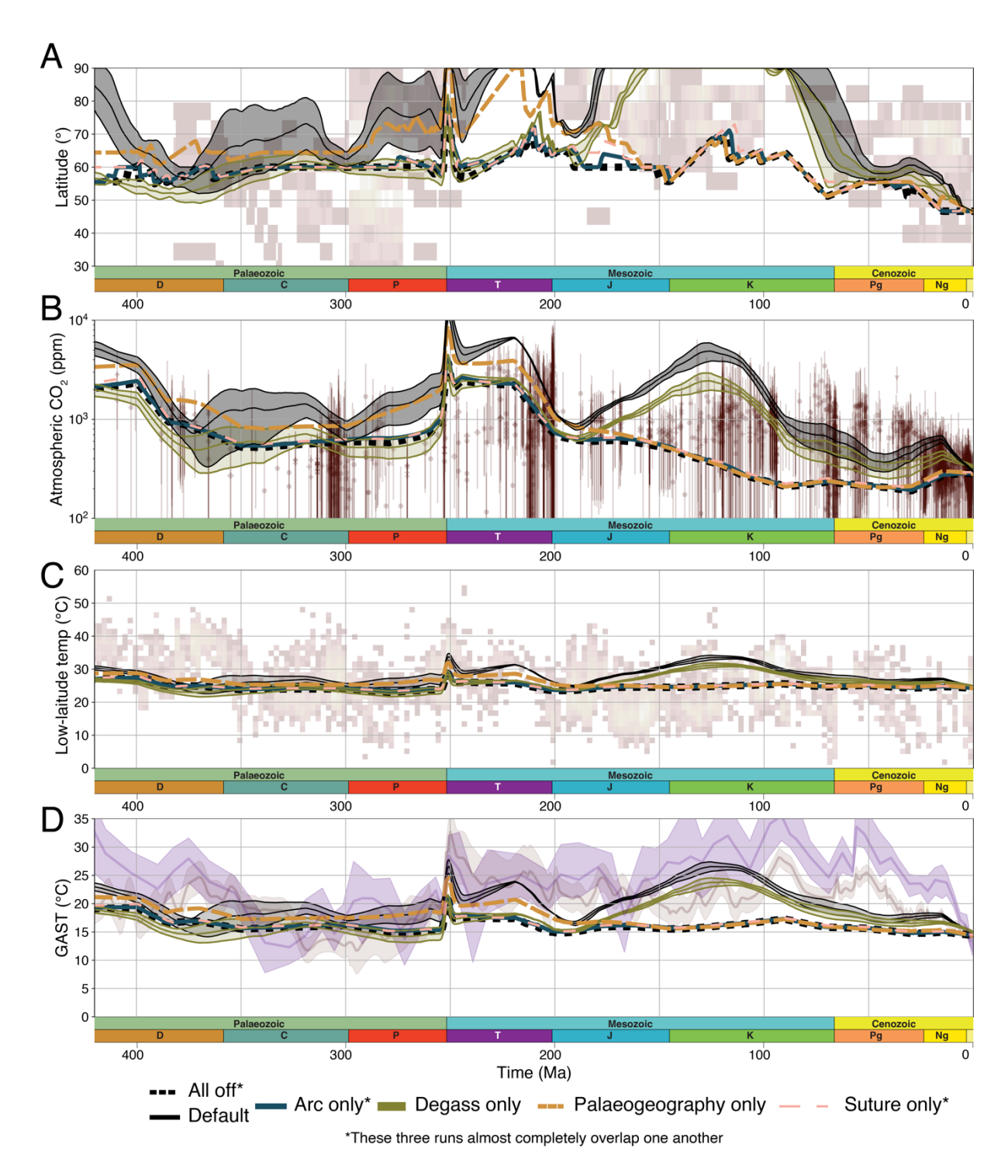


Figure 4: Results of the model where only one driver is turned on. Proxy data in each panel is the same as those shown in Figure 3. The default run (all drivers on) is plotted as black lines with gray-shaded area. The figure shows (A) Ice line, (B)  $pCO_2$ , (C) equatorial average surface temperature, and (D) global average surface temperature of Scotese et al. (pale red) (45) and

Judd et al. (47) (indigo). 'Arc' and 'suture' only refer to the modeled contribution to silicate weathering of continental arcs and ophiolitic bearing sutures, respectively. Note organic carbon burial is still active in these runs.

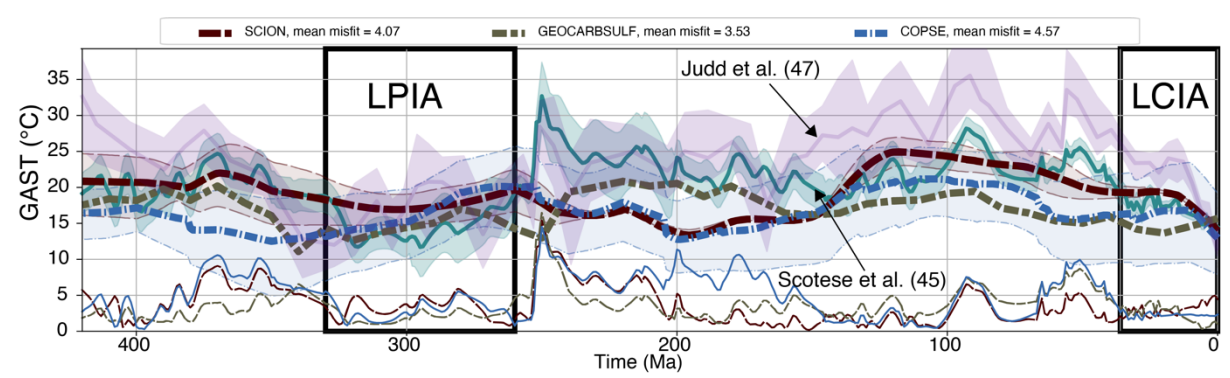


fig. S1. Global average surface temperature prediction of commonly used biogeochemical models (SCION (23), GEOCARBSULF (39), COPSE (27)). Misfit refers to the Wasserstein distance (see methods) between the distribution of each result and the temperature of (45). These misfits are shown as the thin lines towards the bottom of the figure. LPIA: late Paleozoic ice age; LICA: late Cenozoic ice age. Solid green line with envelope is the GAST curve of (45), indigo line with envelope is the GAST curve of (47).

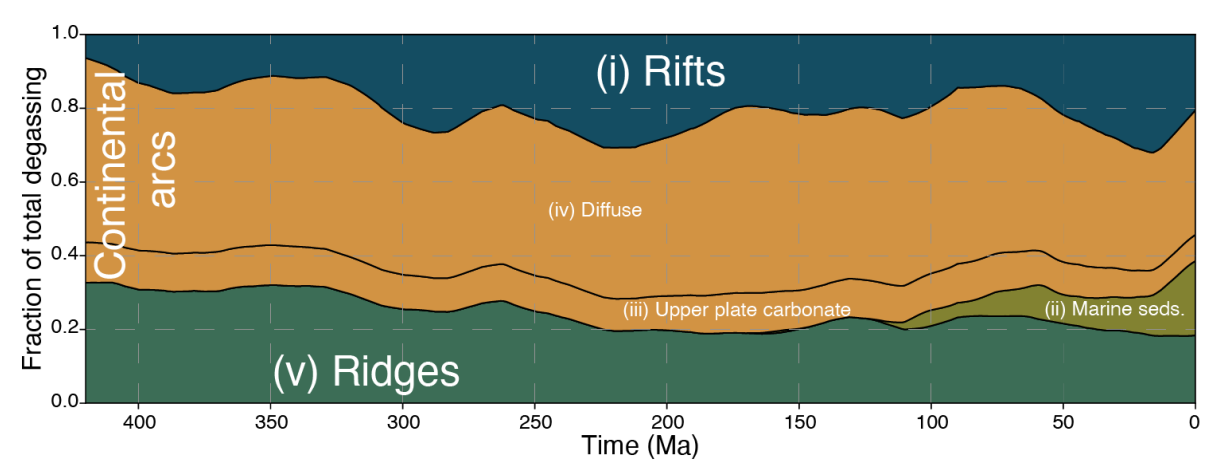


fig S2: Fractional content of total degassing through time from each different source. 'Ridges' refers to mantle degassing along mid-ocean ridges; 'Marine sediments' refers to carbon derived from deep-sea pelagic sediments subducted since the mid-Cretaceous; 'diffuse' refers to low-temperature diffuse degassing around continental arcs (104); 'rifts' refers to continental rifts (95); 'Deep cont. carbon' refers to carbon assimilated from deep crustal sources around continental arcs (106), and 'Shallow cont. seds.' refer to shallow sediments around continental arcs (121).

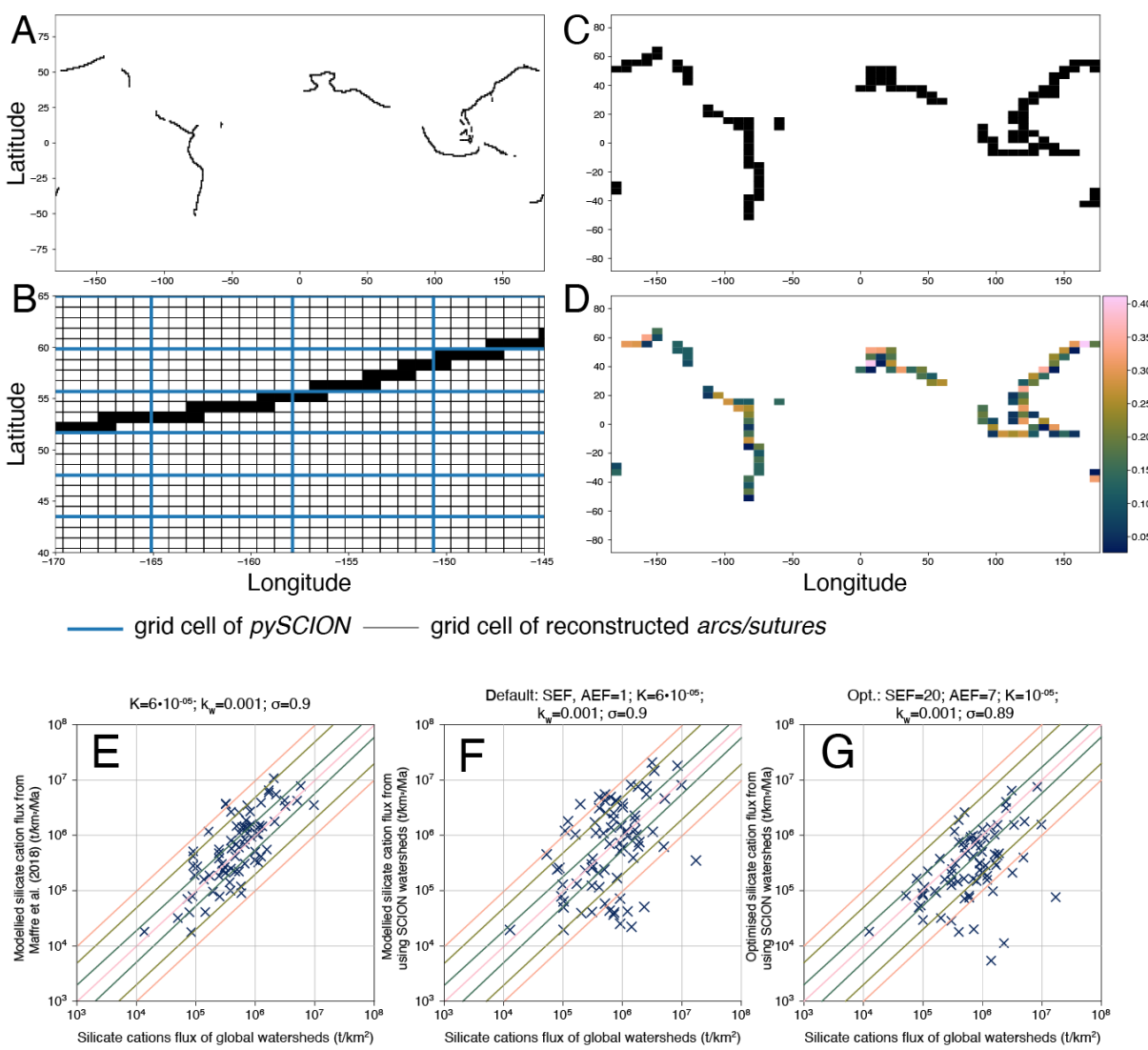
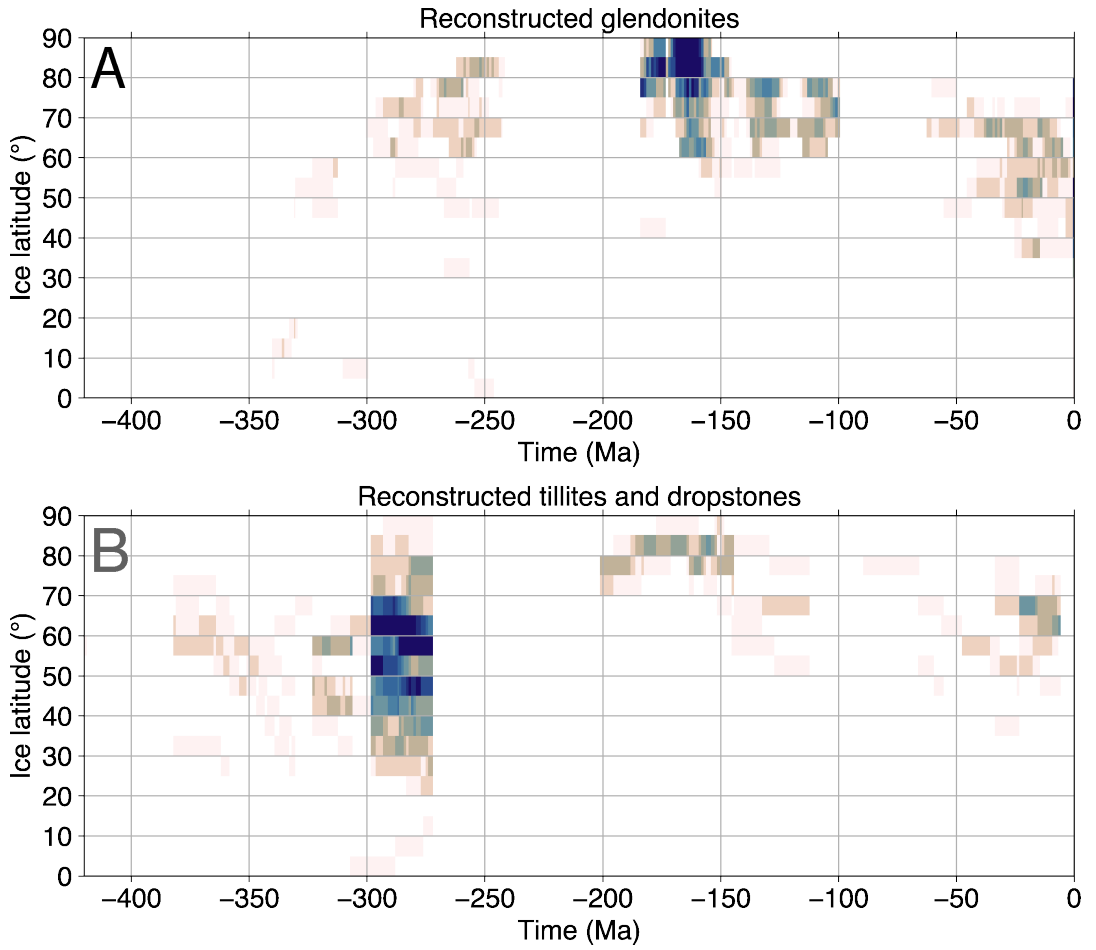


fig S3. Summary of digitization, incorporation and calibration of arcs and ophiolitebearing sutures and their enhanced weathering factors into pvSCION. This figure uses maps of peri-continental subduction zones extracted from (30) at present-day as an example. (A) Digitization of arcs at original resolution (onto a grid spacing of 100 • 100 km). (B) Digitization of arcs at pySCION resolution (onto a grid cell resolution of 7.5° • 4.5°, corresponding to a 48 • 40 grid). (C) Overlay of pySCION grid cells (B) above original resolution grid cells (A). For each pySCION grid cell (blue lines) we sum the area of arc grid cells in the original resolution, then express this as a fraction of total pySCION grid cell area (grid cell area for both resolutions is corrected for latitude). (D) Represents the area-corrected grid cell fraction of continental arcs. Scatterplots showing modeled riverine silicate cation flux compared to what is measured in present-day watersheds, with different erosion and enhancement factors highlighted in the titles. Each point (X) represents a unique watershed. Pink, green, olive and salmon lines represent the 1:1 equivalence line and the 2-fold, 5-fold and 10-fold difference lines, respectively. (E) The 'best-fit' erosion parameters from (40). (F) Unoptimized and default values in the SCION model. (G) Optimized values, including variations in arc and suture enhancement factors from pySCION.



**fig S4: Reconstructed lithological data used to constrain paleoiceline.** Here we split the dataset into its two components: (A) reconstructed glendonites after Rogov et al. (43), and (B) reconstructed tillites and dropstones after Boucot et al. (42).

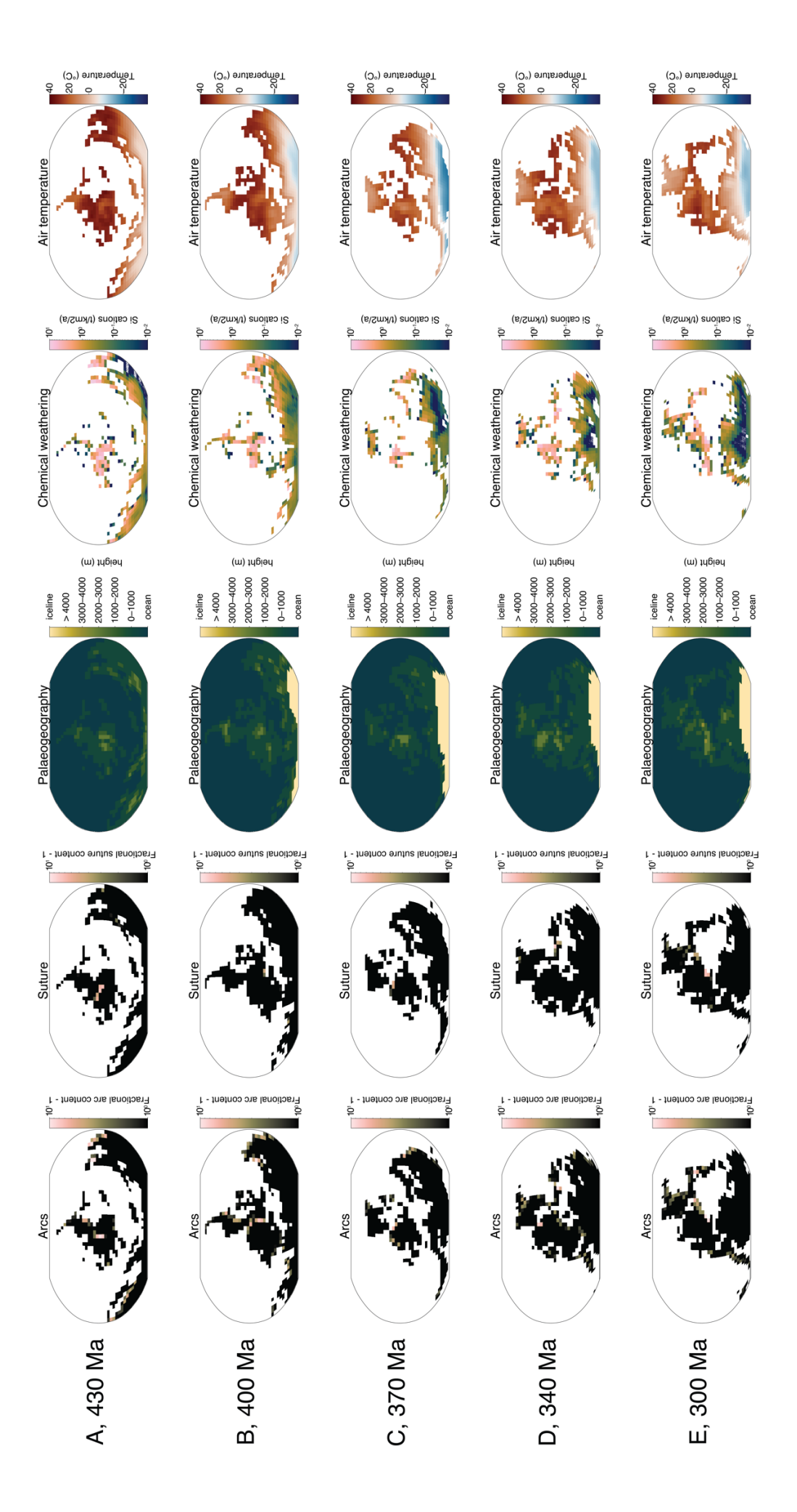
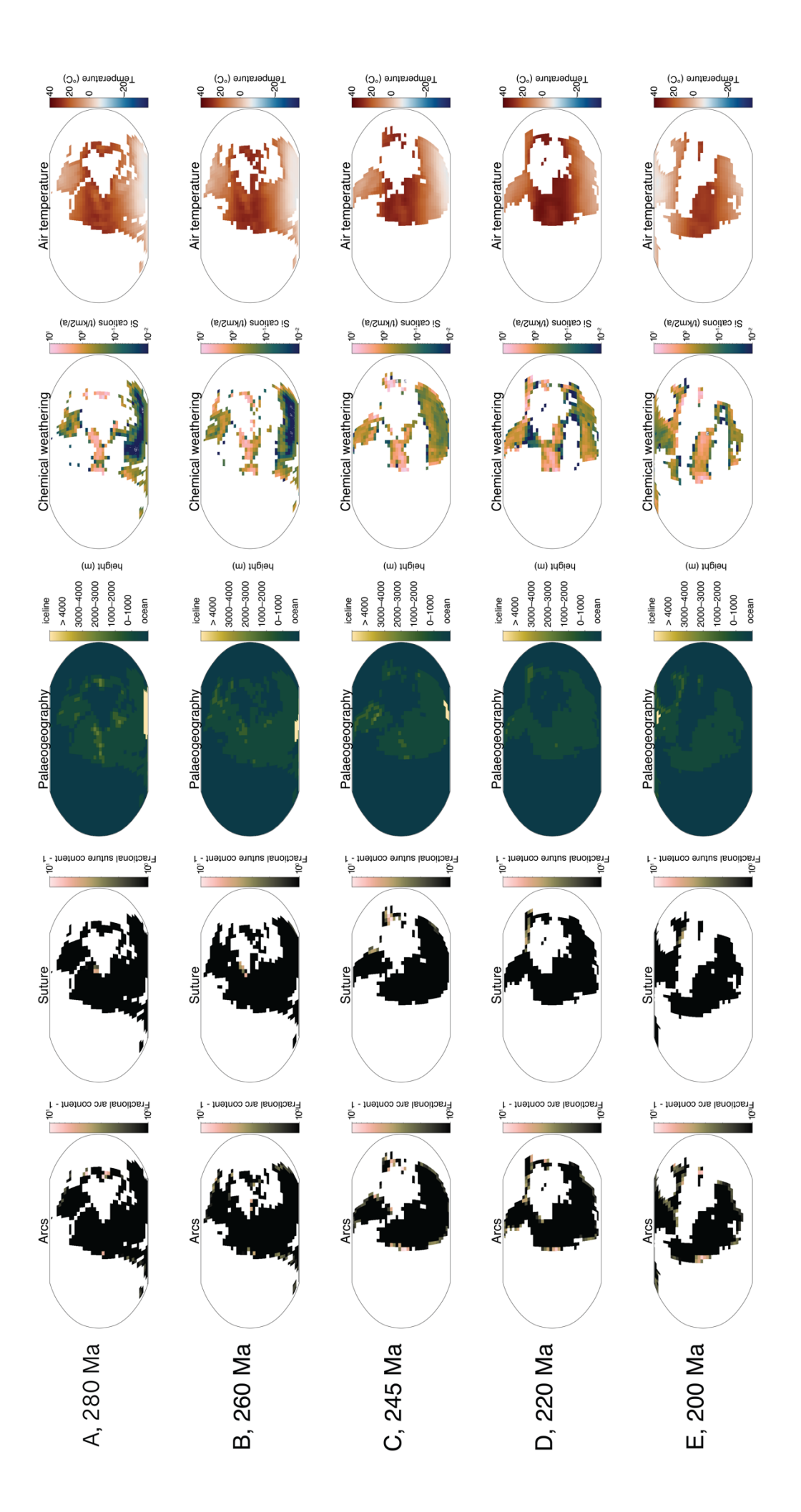
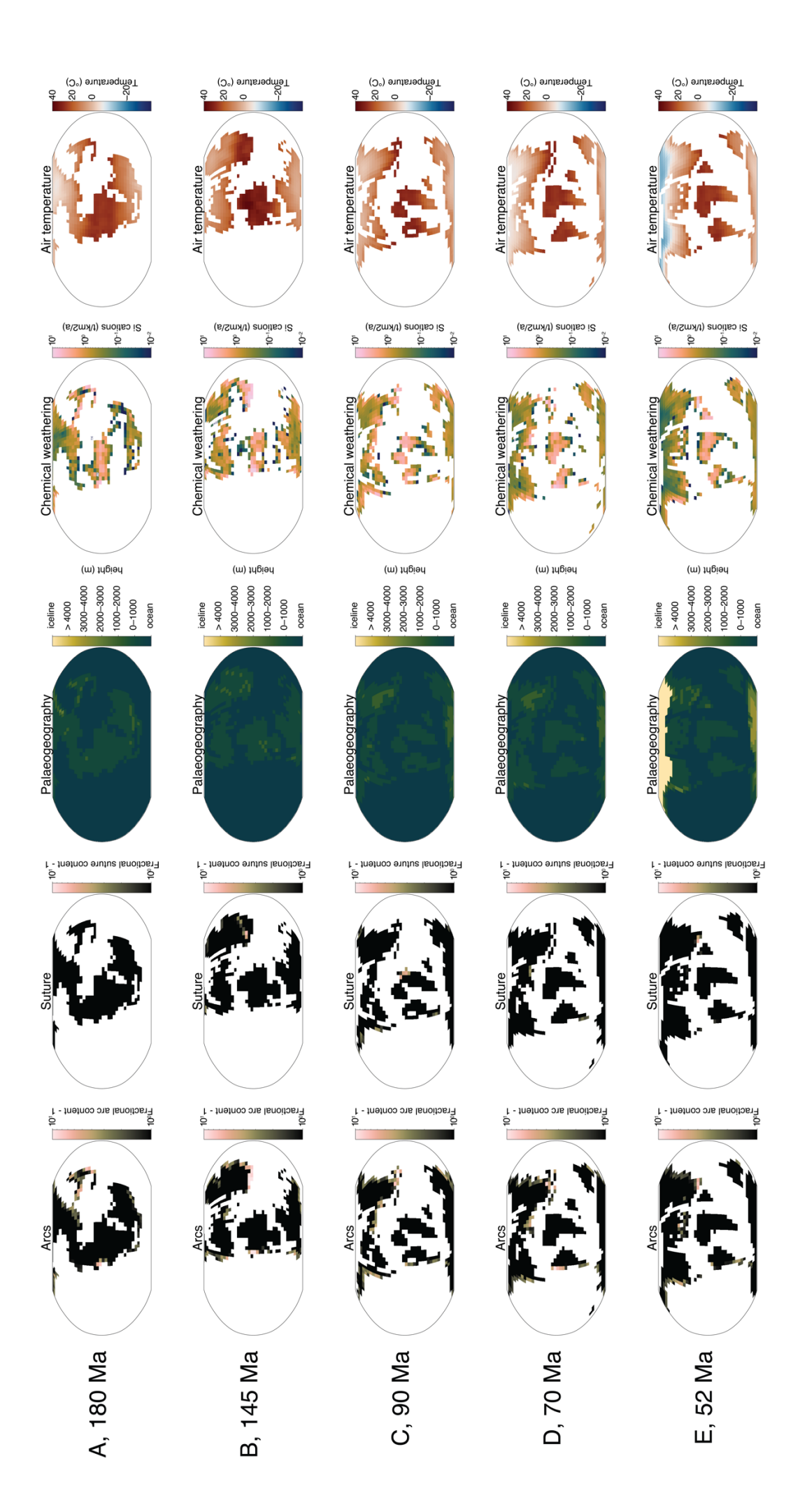


fig S5: Mean spatial inputs and outputs from *pySCION* default run (all drivers on). Organized by grid-timesteps from 430 to 300 Ma as rows with variables as columns. Results at (A) 430 Ma, (B) 400 Ma, (C) 370 Ma, (D) 340 Ma, and (E) 300 Ma. Arcs represent locations and fractional content of peri-continental arcs (subtract 1 from grid-cell value to get fractional content). Sutures represent locations and fractional content of ophiolite-bearing sutures after (9) (subtract 1 from grid-cell value to get fractional content). Paleogeography depicts underlaying land-sea masks and paleotopography used as boundary conditions for both the FOAM climate models that underpin *pySCION* and the spatial parameters that are used to compute runoff and erosion. Chemical weathering represents the sum of all chemical weathering sources (including arcs and sutures). Air temperature is modelled temperature based on calculated  $pCO_2$  level. Note that the iceline is set at -10°C, while colour scale the inflection point is 0°C.



**fig S6: Mean spatial inputs and outputs from** *pySCION* **default run (all drivers on).** Organized by grid-timesteps from 280 to 200 Ma as rows with variables as columns (as with fig. S5). Results at (A) 280 Ma, (B) 260 Ma, (C) 245 Ma, (D) 220 Ma, and (E) 200 Ma.



**fig S7: Mean spatial inputs and outputs from** *pySCION* **default run (all drivers on).** Organized by grid-timesteps from 180 to 52 Ma as rows with variables as columns (as with fig. S5). Results at (A) 180 Ma, (B) 145 Ma, (C) 90 Ma, (D) 70 Ma, and (E) 52 Ma.

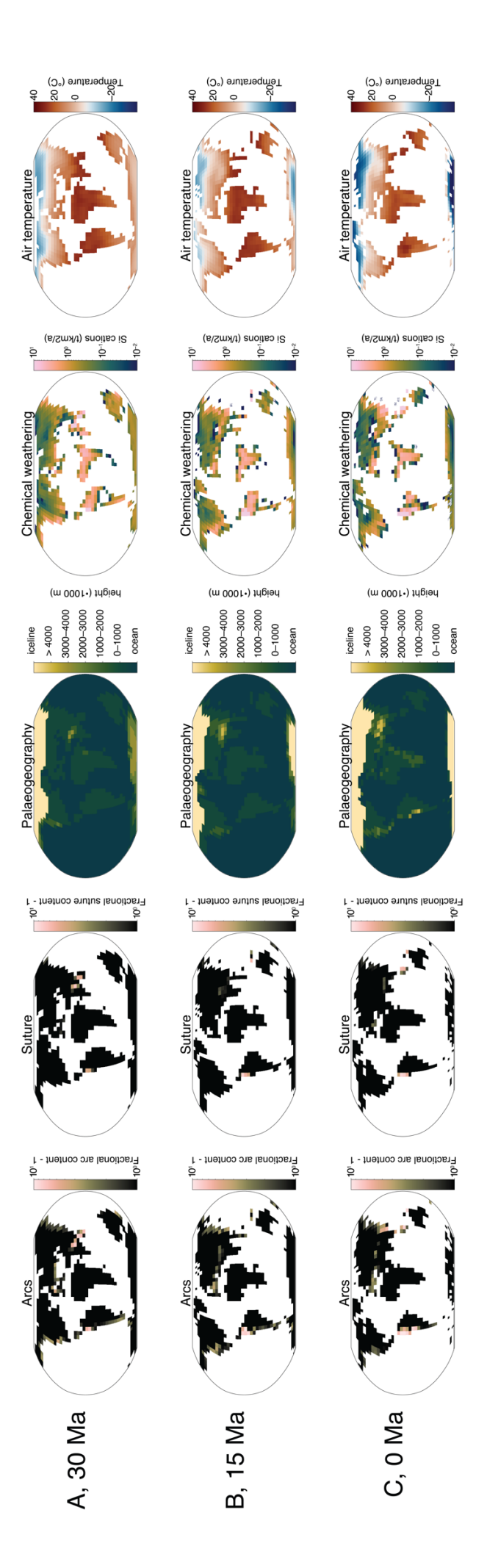


**fig. S8: Mean spatial inputs and outputs from** *pySCION* **default run (all drivers on).** Organized by grid-timesteps from 30 to 0 Ma as rows with variables as columns (as with fig. S5). Results at (A) 30 Ma, (B) 15 Ma, and (C) 0 Ma.

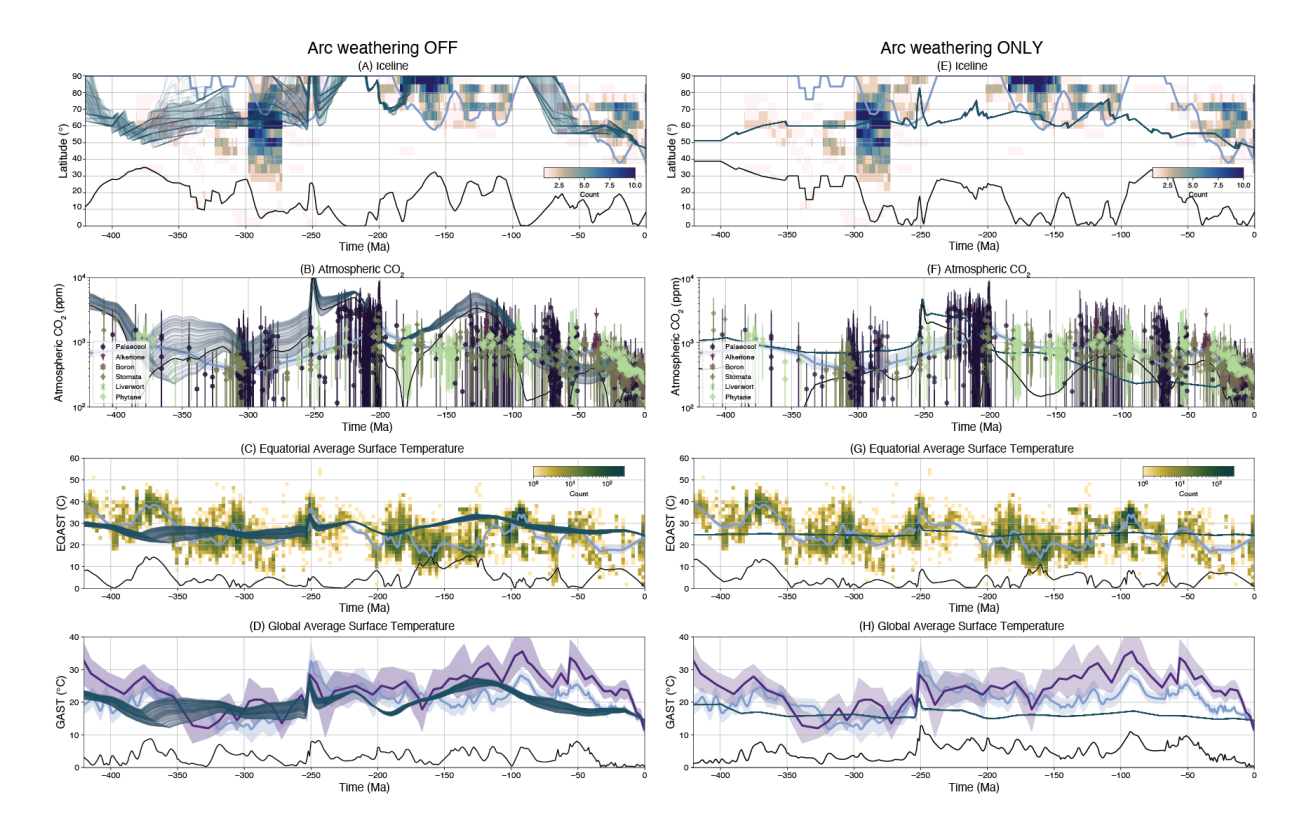


fig. S9: Model run with contribution to silicate weathering cycle from peri-continental arcs and relict arcs 'off' (i.e., no extra contribution) in column 1, and with only their contribution on in column 2. (A and E) iceline extent, with proxy data (42, 43). (B and F)  $pCO_2$  levels with proxy data (57, 58). Equatorial average surface temperature from  $\delta^{18}O(51)$ . (D and H) global average surface temperature, against proxy curves of (45) (blue) and (47) (indigo).

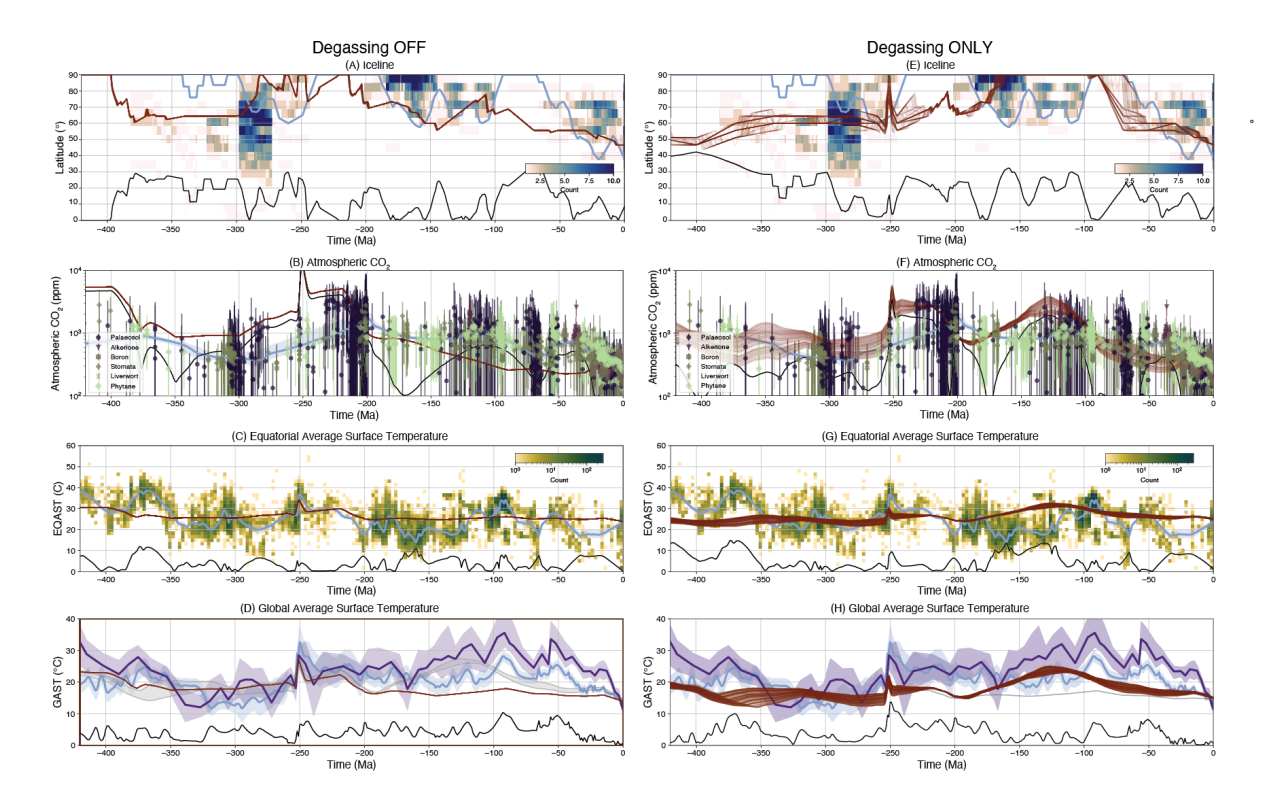


fig. S10: Model run with degassing turned 'off' (i.e., set to present-day levels) in column 1, and with only their contribution on in column 2. (A and E) iceline extent, with proxy data (42, 43). (B and F)  $pCO_2$  levels with proxy data (57, 58). Equatorial average surface temperature from  $\delta^{18}O$  (51). (D and H) global average surface temperature, against proxy curves of (45) (blue) and (47) (indigo).

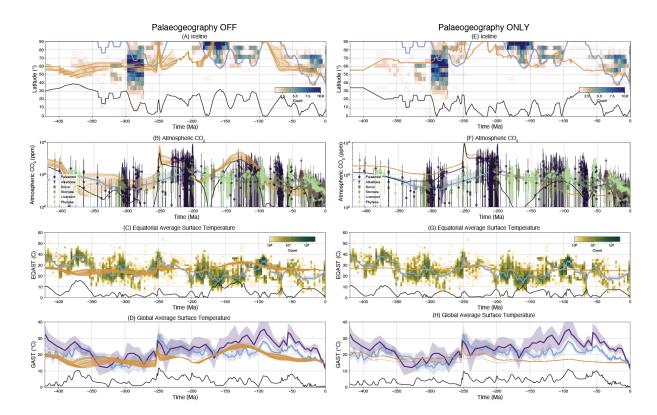


fig. S11: Model run with paleogeographic variation turned 'off' in column 1, and with only their contribution on in column 2. (A and E) iceline extent, with proxy data (42, 43). (B and F) pCO<sub>2</sub> levels with proxy data (57, 58). Equatorial average surface temperature from  $\delta^{18}$ O (51). (D and H) global average surface temperature, against proxy curves of (45) (blue) and (47) (indigo).

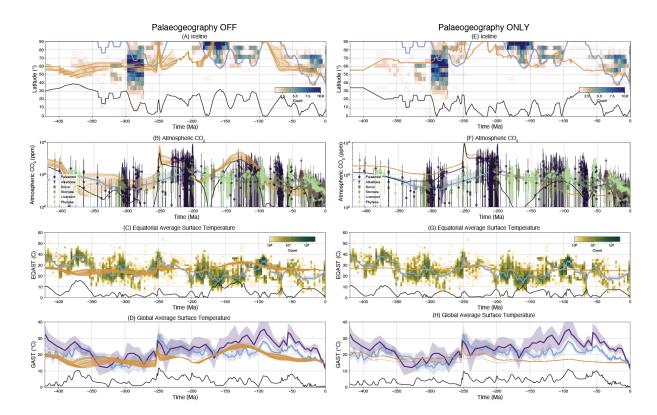


fig. S12: Model run with contribution to silicate weathering cycle from ophiolite-bearing sutures 'off' (i.e., no extra contribution) in column 1, and with only their contribution on in column 2. (A and E) iceline extent, with proxy data (42, 43). (B and F)  $pCO_2$  levels with proxy data (57, 58). Equatorial average surface temperature from  $\delta^{18}O$  (51). (D and H) global average surface temperature, against proxy curves of (45) (blue) and (47) (indigo).

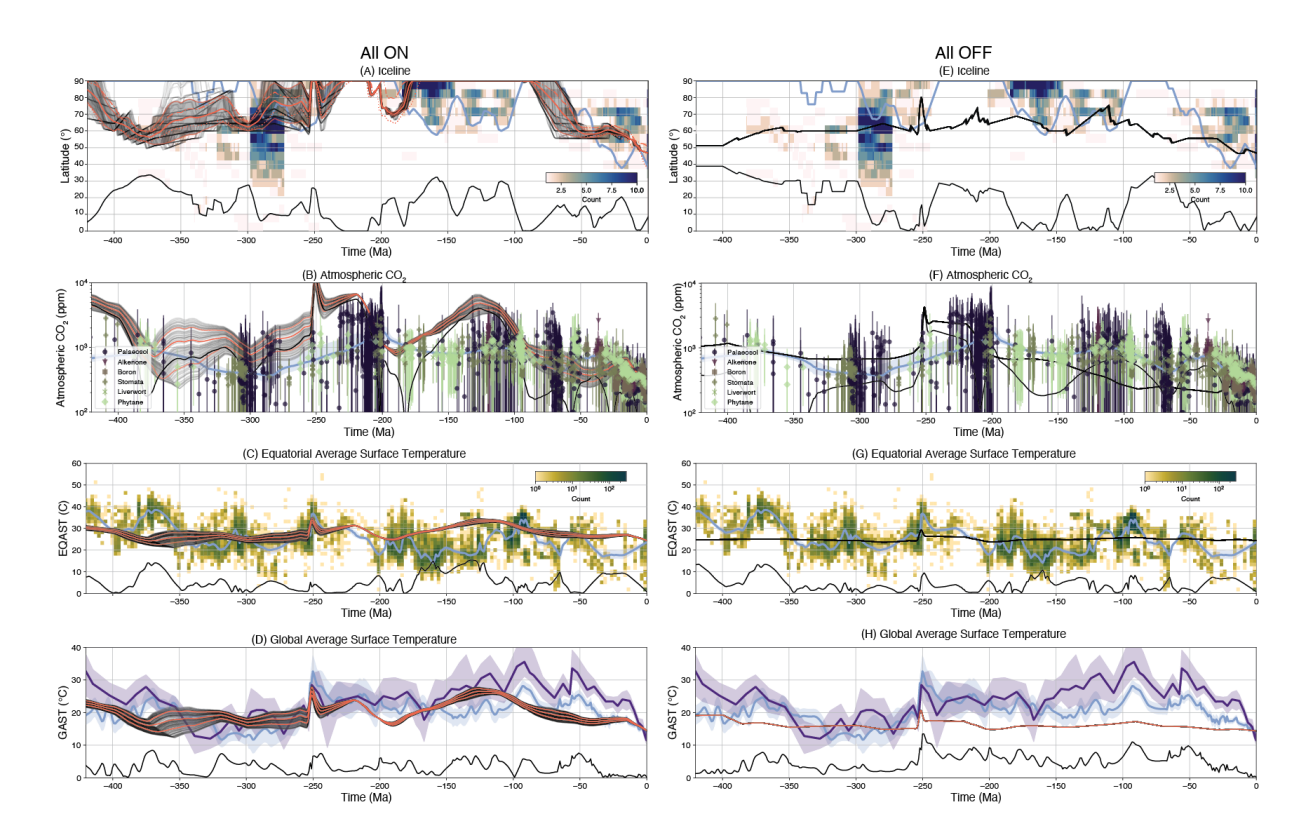


fig. S13: All drivers on (column 1, equivalent to Fig. 2 in main text) and off. (A and E) iceline extent, with proxy data(42, 43). (B and F)  $pCO_2$  levels with proxy data (57, 58). Equatorial average surface temperature from  $\delta^{18}O$  (51). (D and H) global average surface temperature, against proxy curves of (45) (blue) and (47) (indigo).

# (A) Iceline 80 70 Latitude (°) 40 30 20 10 -200 Time (Ma) -250 -150 -400 -350 -300 -100 (B) Atmospheric CO, Atmospheric CO<sub>2</sub> (ppm) -200 Time (Ma) -350 (C) Equatorial Average Surface Temperature 60 50 10<sup>1</sup> Coun <u>()</u> 40 EQAST 10 -300 -200 -150 Time (Ma) (D) Global Average Surface Temperature 40 GAST (°C) -250 -200 -150 -300 Time (Ma)

All ON plus LIP degassing

**fig. S14: 'Default' all drivers on model run including estimated LIP degassing after** (35). We also include estimated sLIP degassing of the Whitsunday Volcanic Province of ~1.67 •  $10^{11}$  moles C/a, assuming a LIP volume of  $2.5 \cdot 10^6$  km<sup>3</sup>, a degassing duration from 120-105 Ma and a similar degassing proportion of the Siberian Traps (122, 123). (A) iceline extent, with proxy data (42, 43). (B)  $pCO_2$  levels with proxy data (57, 58). (C) Equatorial average surface temperature from  $\delta^{18}O$  (51). (D) global average surface temperature, against proxy curves of (45) (blue) and (47) (indigo).

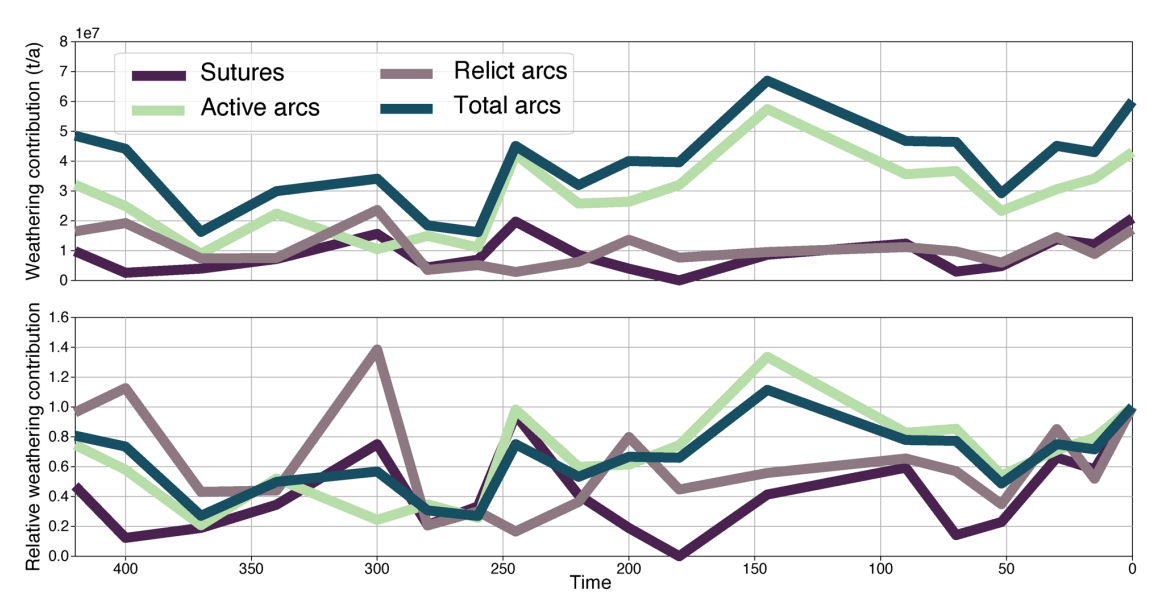


fig. S15: Contributions of our various geological features to the silicate weathering cycle. Values are taken from figs. S5-8.

Supplementary Table 1: Summary of weathering parameters used in our analysis (40, 88). We used an implementation of a least-squares algorithm, comparing against present-day dissolved river loads, to find the optimised value within the given ranges.

Parameter	Purpose	Range of values	Optimized value
K	Inherent characteristic of mineral weathering and dependence on grain size	10-5-10-2	10-5
Kw	Role of water flow	10-6-10-3	10-3
σ	Effect of time on weathering rate	0.6–1.3	0.89
AE	Weathering enhancement due to presence of peri-continental arcs	7–20	7
SEF	Weathering enhancement due to presence of ophiolite-bearing sutures	7–20	20